Report no. changed (Mar 2006): SR-287-UU

NATO
OTAN

Undersea Research Centre
Centre de Recherche Sous-Marine

Mechanisms for subcritical penetration into a sandy bottom: Experimental and modeling results

A. Maguer
E. Bovio
W.L.J. Fox
E. Pouliquen
H. Schmidt

NORTH ATLANTIC TREATY ORGANISATION
ORGANIZATION DU TRAITE DE L'ATLANTIQUE NORD

May 1998
Report SR-287

Report no. changed (Mar 2006): SR-287-UU

Mechanisms for subcritical penetration into a sandy bottom : Experimental and modeling results

A.Maguer, E.Bovio, W.L.J.Fox,
E.Pouliquen, H.Schmidt

The content of this document pertains to work performed under Project 031-1 of the SACLANTCEN Programme of Work. The document has been approved for release by The Director, SACLANTCEN.

Jan L. Spoelstra
Director

intentionally blank page

Mechanisms for subcritical penetration into a sandy bottom : Experimental and modeling results

A.Maguer, E.Bovio, W.L.J.Fox, E.Pouliquen,
H.Schmidt

Executive Summary:

Mines which are completely buried in certain types of ocean sediments are generally considered undetectable for conventional high frequency minehunting sonars. This is due to the very low levels of energy that are transmitted into the sediment for these frequencies at the low grazing angles favored for minehunting operations. Since the attenuative effect of the sediment is less at lower frequencies, some recent work at SACLANTCEN has investigated the possibility of using much lower frequency sonars at low grazing angles in order to enhance the ability to hunt buried mines.

The basic physics of sound penetration into the sediment is a current area of active research, since a good understanding of this phenomenon is essential for designing systems that can effectively hunt buried mines. Several researchers have reported anomalously high levels of sound penetration into ocean sediments when compared to basic theory, and competing hypotheses have arisen in order to explain this effect.

This report presents the results of a recent experiment, part of which was aimed at attempting to explain the mechanism(s) by which anomalously high levels of energy are transmitted into the sediment. Acoustic energy in the frequency band 2-16 kHz was directed toward a sandy seabottom, and buried hydrophones measured the incoming signals. Two different theoretical approaches have been used to model the experimental results. The conclusion is that fundamental sound propagation theory can explain the received levels for frequencies below 5-7 kHz, but that scattering due to the rough nature of the seabed is the dominant mechanism above these frequencies.

Future work in this area will in part concentrate on verifying the results presented in this report, and generalizing for other types of seabeds. Also, buried-target backscattering measurements have been made in the same frequency range, and the results will be reported using the conclusions of this report as a guide. Finally, recommendations for system concepts that can enhance the ability to hunt buried mines will be made based on the results of these studies.

intentionally blank page

Mechanisms for subcritical penetration into a sandy bottom : Experimental and modeling results

A.Maguer, E.Bovio, W.L.J.Fox, E.Pouliquen,
H.Schmidt

Abstract:

This paper presents the results of a recent study whose overall objectives are to determine the mechanism(s) contributing to subcritical acoustic penetration into ocean sediments, and to quantify the results for use in sonar performance prediction for the detection of buried objects. In situ acoustic measurements were performed on a sandy bottom whose geoacoustic properties were carefully identified. A parametric array mounted on a tower moving on a rail was used to insonify hydrophones located above and below the sediment interface. An extensive dataset covering grazing angles both above and below the estimated critical angle and frequencies between 2-16 kHz was acquired and processed. The results are compared to models. For the specific bottom type examined, it is shown that for frequencies below 5-7 kHz the sound field into the sediment due to subcritical insonification is dominated by the evanescent field, while scattering due to the surface roughness is the dominant mechanism for higher frequencies. However, it must be mentioned that the contribution of the roughness scattering was always found to be lower than the one obtained at lower frequency with the evanescent wave.

Keywords: seafloor ○ scattering ○ sound penetration ○ kirchhoff ○ small perturbation ○ evanescent wave ○

Contents

1

Introduction

Sonars are important tools for the detection of buried objects such as mines, pipelines, containers or shipwrecks for example. The detection of such objects by conventional high-frequency sonars is limited by the physics of high-frequency sound penetration into the sediment.

Other research institutions have proposed buried object detection and classification systems using lower frequencies and normal incidence or swath approaches designed to work above to the critical grazing angle. The NATO SACLANT Undersea Research Centre (SACLANTCEN) has investigated an alternative approach to buried object detection using a parametric source (with secondary frequencies in the range 2-16 kHz) at low grazing angles, including below the critical grazing angle. This approach would provide larger area coverage.

In order to pursue this approach, it is very important to understand the basic physics underlying the penetration of acoustic energy into ocean sediments. Snell-Descartes analysis [1] predicts evanescent energy propagating in the sediment for subcritical grazing angles. Recent investigations ([2], [3]) have shown experimental evidence of "anomalous" acoustic penetration below the critical grazing angle due to other mechanisms. Several theoretical explanations have been promulgated for this phenomenon, including:

- 1. the roughness of the water-sediment interface [4],
- 2. the effect of using a narrow beamwidth [5],
- 3. the porous nature of the sediment that leads to a second "slow" compressional wave with a wave speed less than the speed of sound the water in [6],
- 4. the volume inhomogeneities within the sediment that scatters the evanescent wave. [7],[8],[9],[10]

The goal of this work is to investigate the cause of acoustic penetration into ocean sediments, and to quantify the effect to aid in our buried object detection sonar design and performance prediction.

The acoustic measurements addressing the penetration hypotheses were performed using the TOPAS parametric source [13] covering the frequency range 2-16 kHz for the secondary frequencies and the 35-45 kHz for the primary frequencies. The sonar was located 8 meters above the interface and displaced horizontally from 12.5 to 30 meters (grazing angles from 32.6 to 14.9 degrees) from a set of hydrophones both in the water column and into the sediment. Environmental measurements were performed, such as coring and sub-bottom profiling, in order to characterize the bottom in which the hydrophones were buried. An underwater digital video camera was also used by divers to have some idea about the roughness of the bottom.

This report describes the results obtained for hydrophones deployed at two different depths into the sediment (30 and 60cm) as a function of the grazing angle and of the frequency of the incident beam.

Section 2 is dedicated to the description of the experimental set-up. A brief description of the equipment used, and especially of the rail facility specially designed for this kind of experiment is given [14]. The results and the interpretation of the cores and of the boomer survey are also given.

Section 3 describes the results obtained after processing the collected data. The variation of the Sound Pressure Level and therefore the penetration ratio (defined as the magnitude of the ratio in dB of the acoustic pressure in the sediment to the incident pressure in the water at the same frequency) within the sediment (including the loss at the interface water-sand) are given as a function of the grazing angle, the frequency and the burial depths of the hydrophones. Both frequency ranges (2-16 kHz and 35-45 kHz) of the sonar are considered.

Section 4 presents the different theoretical approaches and the associated numerical models used for comparison with the data. The first model uses a combination of the standard OASES code and a perturbation approach to compute the 3D scattered field in the ocean waveguide [11]. The second model corresponds to a 3D simulation of the penetration ratio using the Helmholtz-Kirchhoff theory on a rough surface [12]. The two models used the same statistically generated rough surface of similar direction to that observed by divers during the at-sea experiment. A comparison of the data to the models is therefore performed which yields the conclusion: for the specific bottom type examined, subcritical penetration is dominated by the evanescent field below 5-7 kHz, while scattering due to the surface roughness is the dominant mechanism for higher frequencies. Also the analysis shows that the frequency dependence of sound speed predicted by the Biot theory may be important in porous sand sediments, primarly because of the associated change in critical angle.

Section 5 summarizes the effort and gives directions for future work.

2

Experimental Setup

2.1 Equipment and geometry

The parametric sonar used for this experiment was the SIMRAD TOPAS (TOpographic PArametric Sonar) [13]. A short single pulse is obtained by transmitting a weighted HF-burst at the primary frequency. The TOPAS transducer consists of 24 staves, electronically controlled to form a beam in a selected direction. It covers the frequency range 2-16 kHz for the secondary frequency and the 35-45 kHz for the primary frequency. The transmitting source level is approximately 238 dB for the primary frequency. The source levels obtained at different frequencies vary from about 190 to 213 dB/1 m ref. μPascal at 1 m in the 2 to 16 kHz frequency band.

The broadband integrated source level obtained for different Ricker pulses of the low-frequency generated by the parametric sonar are given in Table 1, while Fig. 1 shows graphically the temporal signals of the Ricker pulses with their associated spectra.

Pulse	**Beam Width HF/LF (-3dB)**	**Band Width LF (-3dB)**	**LF SL (dB/1μPa)**	**HF SL (dB/1μPa)**
Ricker 8kHz	3° / 4°	6 kHz	201	238
Ricker 5kHz	3° / 4°	7 kHz	203.8	238
Ricker 4kHz	3° / 4°	6 kHz	202.6	238

Table 1 *Source level measurements*

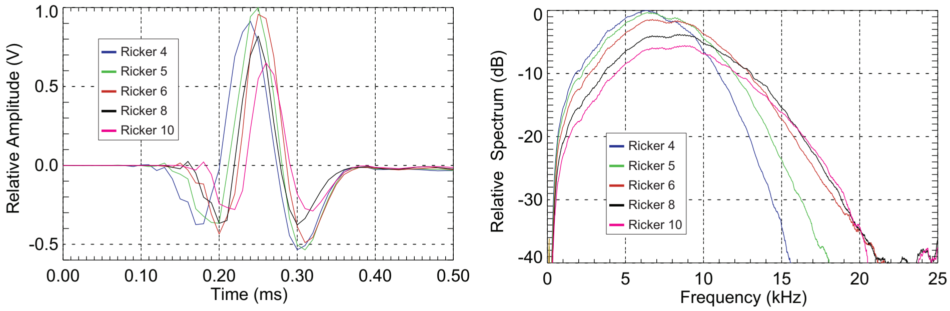

Figure 1 *Ricker pulses and their spectra*

It must be noticed that no strong difference are observed bteween the different Ricker pulses generated by the TOPAS parametric sonar. The main differences are the central frequency and the bandwidths of the generated signals.

A complete calibration of the TOPAS transmitter may be found in [15], while a description of the main functionalities of the TOPAS may be found in the operation manual from Simrad [13].

The experimantal set up for the penetration measurements is shown in Fig. 2.

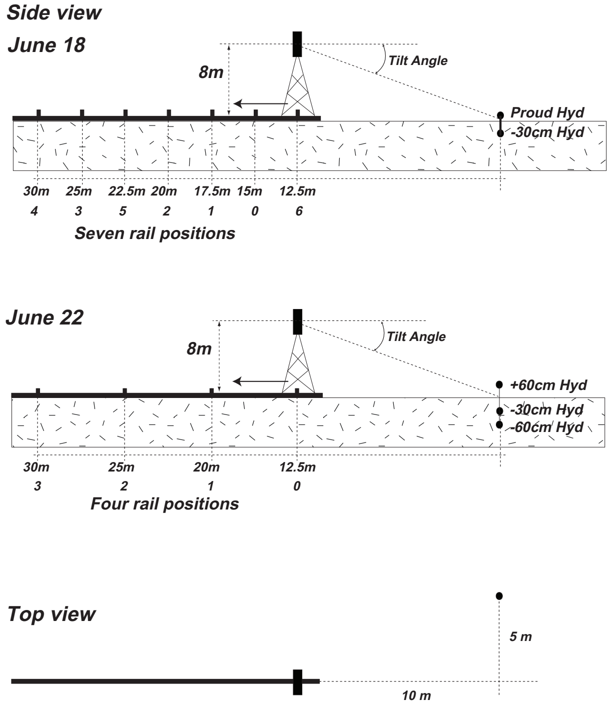

Figure 2 *Experimental Setup*

For acquisition under variable conditions of trial geometry, the transmitter was mounted on a variable-height tower fixed to 8m for this experiment. The tower in turn was mounted on a 24 m linear rail deployed on the bottom, along which its position could be precisely controlled using a pneumatic motor. The TOPAS transmitter was mounted in a Pan-and-Tilt assembly with a MRU (Motion Reference Unit) so that arbitrary transmission directions could be accurately measured. A detailed description of the experimental set-up may be found in [14].

Fig. 3 shows the structure used to support the TOPAS parametric sonar. Note the vertical and horizontal Pan-and-Tilt motors which were essential for the accurate steering of the TOPAS sonar on the buried hydrophones. The 16-element array was used as a receiver for a different portion of the trial dealing with the detection of buried targets.

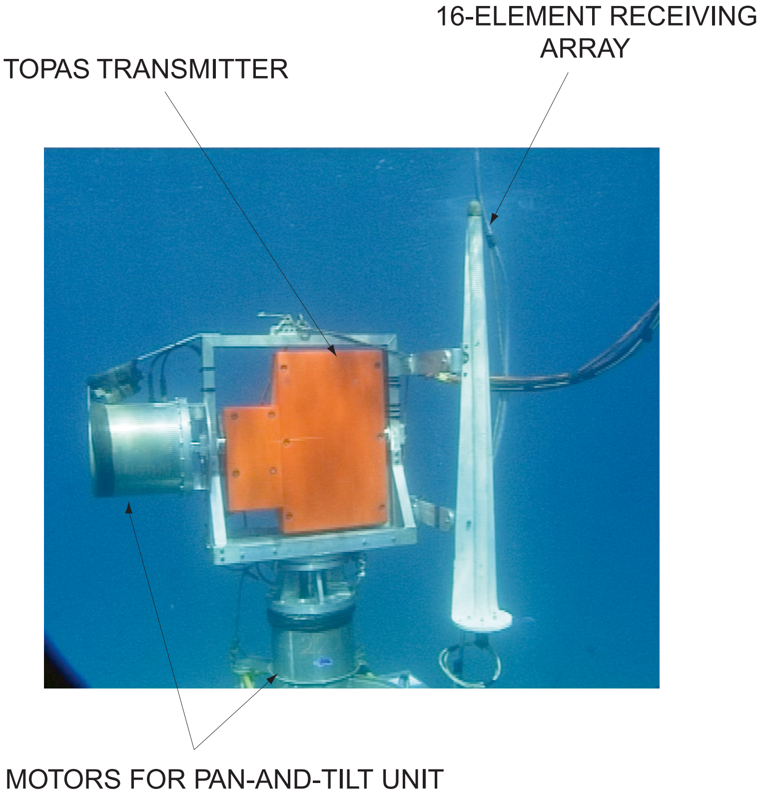

Figure 3 *TOPAS parametric sonar with Pan-and-Tilt unit*

Fig. 4 shows the tower on which the sonar is mounted and the structure with four legs providing stability. This structure was mounted on a small trolley which is running on the rail. An underwater video camera was mounted on the structure to accurately measure the position of the sonar on the rail.

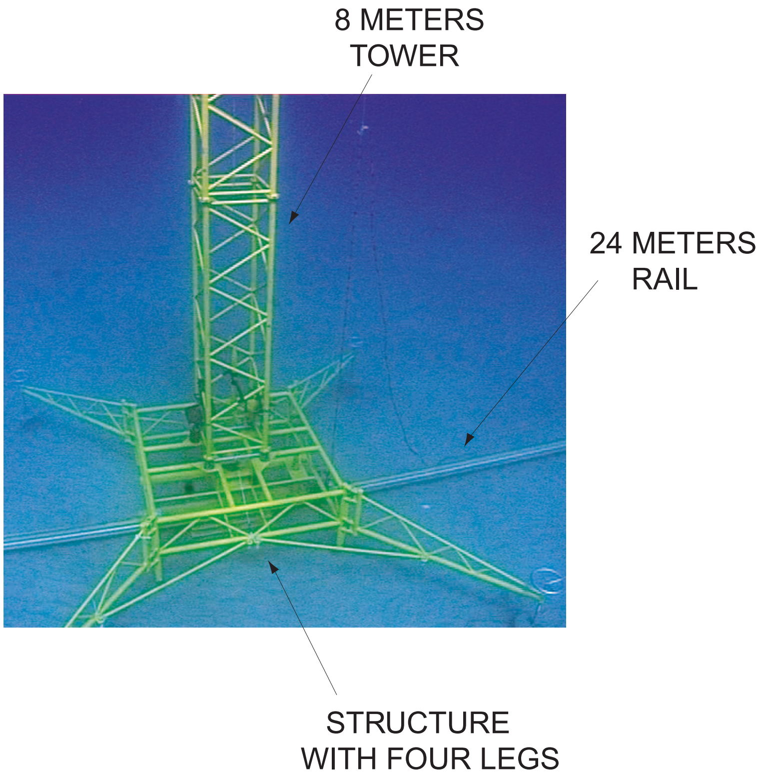

Figure 4 *Tower mounted on rail laying on the bottom*

During the first day (June 18th) of this phase of the experiment, the first hydrophone was put on the bottom and the second buried into the sandy sediment at -30 cm depth. However, the hydrophone in the water column was too close to the bottom, and it was not possible to separate in time the signal received from the direct path from that received from the bottom bounce. It was therefore decided to change the geometry for the second day (June 22nd). The hydrophone in the water column was moved to 60cm above the sea floor. Two hydrophones, instead of one were buried into the sediment at -30cm and -60cm respectively.

Different grazing angles were achieved by moving the tower along the rail. The direction of the transmitter in the horizontal plane was carefully adjusted by mechanically moving the pan unit until the maximum signal was received on the hydrophones. Both primary and secondary frequencies of the parametric sonar were received by the data acquisition system shown in Fig. 5. The range from the sonar to the hydrophones was far enough for the truncation of the primary near field by the water-sediment interface not to play a part in acoustic penetration [16].

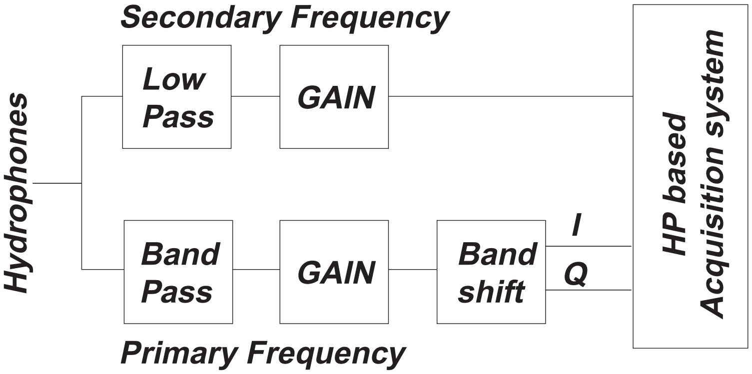

Figure 5 *Data Acquisition System*

Reson hydrophones (type TC4034) were used for all the measurements. A preamplifier was specifically designed at Saclantcen to account for the difference in source level between the primary and the secondary frequency of the TOPAS. Particular attention was given to the design of a filter which should have a linear phase and very low inter-modulation level, and which would therefore prevent any generation of electronic low-frequency signal by the inter-modulation of pairs of primary frequencies within the band.

Two types of measurements were performed at different positions of the tower along the rail: moving tilt and fixed tilt.

In the moving tilt case, signals were transmitted at a fixed interval while the tilt unit mechanically swept a sector in the vertical plane of approximately 40 degrees centered on the direction of the receiving hydrophones. In the fixed tilt case, the vertical angle of transmission was first determined by mechanically moving the tilt unit in the vertical plane until the maximum signal was received on the hydrophones, and subsequently a series of pulses were transmitted keeping the tilt unit fixed. The "maximum" signal was estimated by observing the change in received amplitude on an analog oscilloscope.

The moving tilt experiment was aimed at the measurement of the TOPAS beampattern in the vertical plane at primary and secondary frequencies, while the fixed tilt experiment was aimed at the measurement of the transfer function of the sediment.

Table 2 and table 3 lists the signals transmitted for both experiments on the first day and the second day, respectively.

Table 2 *List of transmitted signals and corresponding geometries during day June 18th*

Rail Pos.	*Range (m)*	*Tilt (deg)*	*Run Type*	*Signals*
0	15.0	-29.9	Fixed Tilt	Ricker 5
		-50 to -10	Moving Tilt	Ricker 5, 8, 10, 4, LFM 2-10 10ms
1	17.5	-24.2	Fixed Tilt	Ricker 5
		-50 to -10	Moving Tilt	Ricker 5, 8, 10, 4, LFM 2-10 10ms
2	20.0	-21.0	Fixed Tilt	Ricker 5
		-50 to -10	Moving Tilt	Ricker 5, 8, 10, 4, LFM 2-10 10ms
3	25.0	-16.9	Fixed Tilt	Ricker 5
		-50 to -10	Moving Tilt	Ricker 5, 8, 10, 4, LFM 2-10 10ms
4	30.0	-14.0	Fixed Tilt	Ricker 5
		-50 to -10	Moving Tilt	Ricker 5, 8, 10, 4, LFM 2-10 10ms
5	22.5	-19.3	Fixed Tilt	Ricker 5
		-50 to -10	Moving Tilt	Ricker 5, 8, 10, 4, LFM 2-10 10ms
6	12.5	-29.9	Fixed Tilt	Ricker 5
		-50 to -10	Moving Tilt	Ricker 5, 8, 10, 4, LFM 2-10 10ms

Table 3 *List of transmitted signals and corresponding geometries during day June22nd*

Rail Position	*Range (m)*	*Tilt (deg) Hyd+60*	*Tilt (deg) Hyd-30*	*Tilt (deg) Hyd-60*	*Run Type*	*Signals*
0	13.0	-28.4	-30.5	-33.1	Fixed Tilt	Ricker 5
		-50 to -10			Moving Tilt	Ricker 5, 8, 4, LFM 2-10 10ms
1	20.0	-20.1	-21.7	-23.1	Fixed Tilt	Ricker 5
		-50 to -10			Moving Tilt	Ricker 5, 8, 4, LFM 2-10 10ms
2	25.0	-16.7	-18.1	-18.5	Fixed Tilt	Ricker 5
		-50 to -10			Moving Tilt	Ricker 5, 8, 4, LFM 2-10 10ms
3	30.0	-13.9	-14.5	-14.5	Fixed Tilt	Ricker 5
		-50 to -10			Moving Tilt	Ricker 5, 8, 4, LFM 2-10 10ms

2.2 Bottom properties

The experiment was performed on a sandy bottom in 10 meters water depth in the Biodola Gulf on the North side of Elba Island.

2.2.1 Coring results

Cores were collected to measure the sound speed in the sediment and to determine the characteristics of the sediment in terms of porosity, grain size, composition and density.

The measured sound speed into the sediment was found to be 1720m/s which means a critical angle of 28 degrees taking into account a sound speed in the water equal to 1525m/s. Note that this sound speed was measured with laboratory equipment operating at 200 kHz. The relevance of this measurement to the low-frequency penetration is an important issue which will be addressed in Section 4.

The composition of the sediment is given in Table 4.

Table 4 *Biodiola bottom composition*

	Gravel	*Sand*	*Silt*	*Clay*
Percentage (%)	0	97.4	1.3	1.4

The average density and porosity were found respectively equal to 1.92 and 44.55 %. The average grain size was of the order of 2.28 (in Φ units, which corresponds to 0.2 mm) corresponding to the classification of fine sand.

2.2.2 Sub-bottom profiling

A sub-bottom profiling ("boomer") survey was performed in the area before burying the hydrophones. The following profile was found:

According to the 1720m/s sound speed measured into the sediment with the coring measurements, the first layer of sand was approximately 1.8 meters thick.

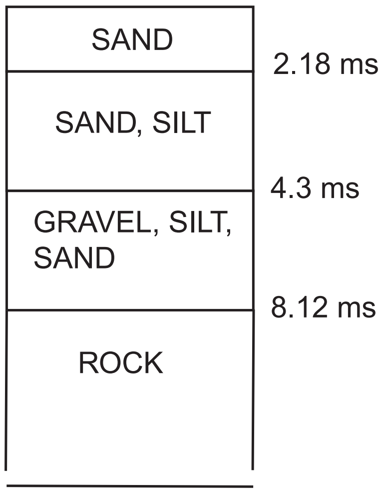

Figure 6 *sub-bottom profiling characteristics*

2.2.3 Roughness Measurements

The measurement of the bottom roughness was performed by divers who took measurements of the sand ripples height and wavelength. It was found that the rms roughness height was of the order of 1 to 2 cm. The sand ripples wavelength was estimated to be 20 cm. Further experiments will have to consider some measurement system such as stereophotography which should provide a more precise spectral characterization of the bottom roughness.

3

Experimental results

3.1 Received signals in the time domain

Figure 7 shows examples of the signals received on the three hydrophones (one 60cm above the bottom, and two buried at 30cm and 60cm respectively, into the sediment) at two different grazing angles. The first column corresponds to the supercritical 30° case while the results to the right correspond to 14 degrees which is the subcritical case.

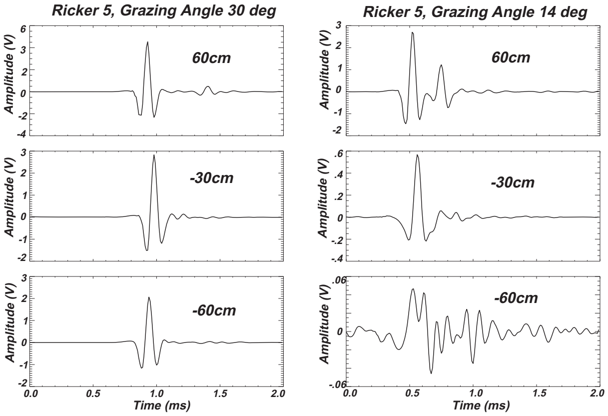

Figure 7 *Examples of 5 KHz Ricker pulse received at different depths and grazing angles*

For the hydrophone located 60cm above the sediment two different signals may be observed corresponding to the direct and bottom-bounce arrivals. For 30 degrees grazing angle, which corresponds to the super-critical case, all the signals received on the different hydrophones (either in the water column or buried) look similar in shape. The only difference is a slight difference in the amplitude which is decreasing with the increase of the burial depth of the hydrophones. For 14 degrees grazing angle, it may be observed that the received signals are changing in shape with the increase of the burial depth. In fact, on the 60cm buried hydrophone, the shape of the incident Ricker pulse is not identifiable anymore. A lower frequency content is observed on the first signal received on the hydrophone (it is better seen on the 30cm buried hydrophone) which means that the higher frequencies of the signal were more attenuated. Moreover, it may be observed that the received signal on the

-60cm hydrophone consists of a succession of signals corresponding to the scattering due to the sea floor. A strong attenuation may aslo be observed in the amplitude of the received signals with the increase of the burial depth.

3.2 TOPAS Beam Pattern

A measurement of the TOPAS beams (both at low-frequency and at high-frequency), which are necessary for the models, was performed using the Pan-and-Tilt facility of the equipment.

A detailed description of the way of how the beam patterns were computed is given in Annex **??**.

3.2.1 Secondary frequency

The 3dB beamwidth of the TOPAS beam pattern derived from the signals shown in Annex **??** has been measured for the 4 different positions of the rail and is shown in Fig. 8 for each hydrophone.

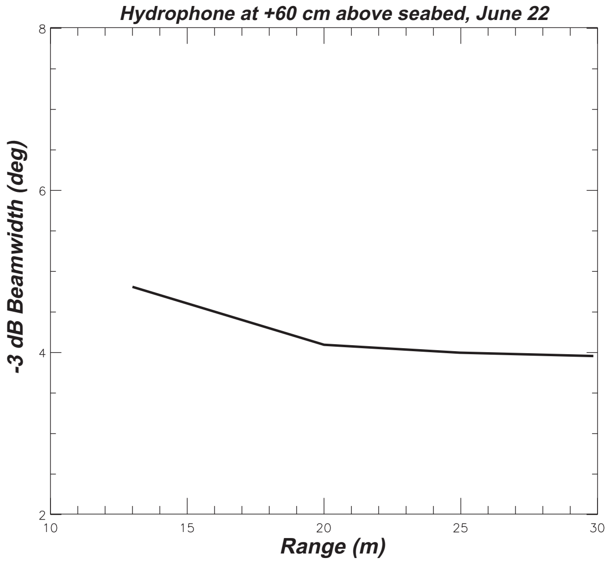

Figure 8 *Beamwidth of the TOPAS secondary frequency beam pattern versus transmitter range*

It can be observed on this figure that the beamwidh of the TOPAS is not constant with range. In fact, because the sonar is parametric a given range is necessary to have the complete generation of the virtual end-fire array giving rise to the low-frequency component. On this figure, a range of 20 meters is found to be necessary at the minimum to get the expected beamwidth.

3.2.2 Primary frequency

In Annex A, Fig. 35 shows the primary frequency beampattern measured on the hydrophones for all rail positions.

The 3dB beamwidth of the TOPAS beam pattern derived from the signals shown in Annex **??** is shown in Fig. 9 for each hydrophone.

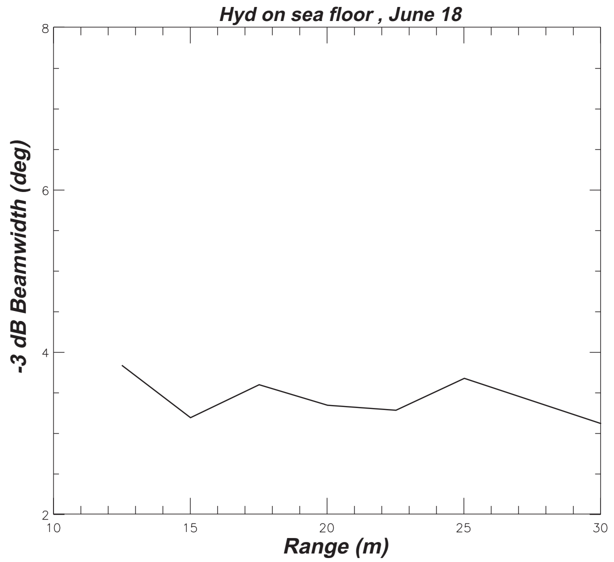

Figure 9 *Beamwidth of the TOPAS primary frequency beam pattern versus transmitter range*

The beamwidth of the primary frequency of the TOPAS parametric sonar is found to be independent of the range and of the order of 3.5 degrees.

3.3 Penetration ratio into the sediment

3.3.1 Penetration ratio versus frequency

In order to estimate the attenuation of the sound wave propagating into the sediment, the sea floor has been modeled as an input/output system where the input is the signal measured on the free field hydrophone, and the output is the signal received on the hydrophones buried into the sediment, as shown in Fig. 10.

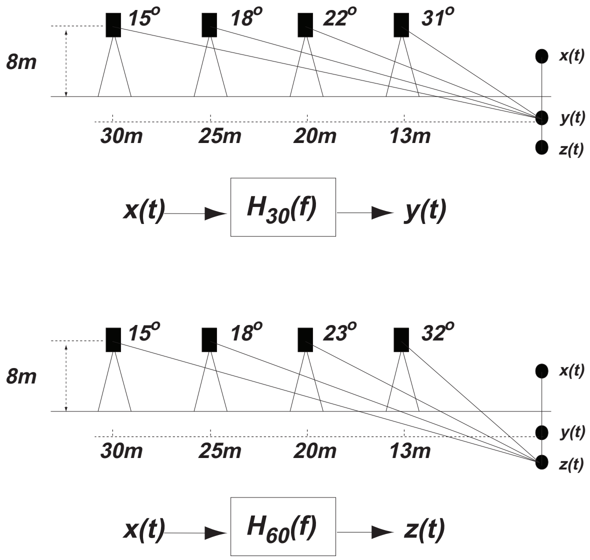

Figure 10 *Model of the sediment penetration ratio*

The penetration ratio is defined as the hydrophone pressure measured at the buried hydrophone (either z or y) divided by the incident pressure (x) in the water column in the absence of the bottom interface.

$$H_{30}(f) =< \frac{|Y(f)|^2}{|X(f)|^2} > \qquad H_{60}(f) =< \frac{|Z(f)|^2}{|X(f)|^2} > \tag{1}$$

Where $X(f)$, $Y(f)$ and $Z(f)$ are respectively the energy spectrum of the signals received on the free field hydrophone, the -30cm buried hydrophone and the -60cm buried hydrophone. The symbol <> means an integration over consecutive pings.

However, instead of using the signal received on the hydrophone in the water a synthetic replica (previously measured during another experiment) was used with the advantage of having a reference signal not fluctuating too much from one ping to another and moreover not affected by any bottom bounce.

Fig. 11 shows the penetration ratio in dB for all positions of the transmitter.

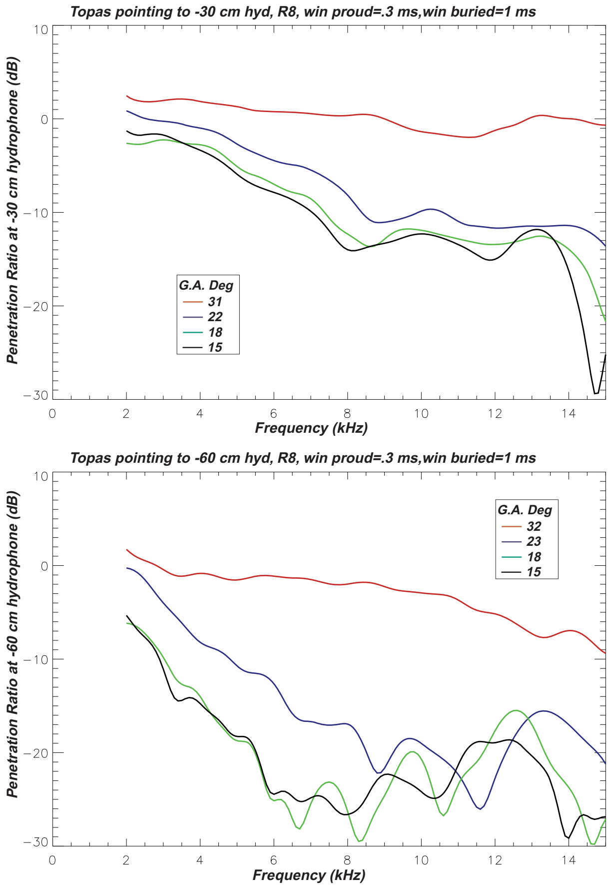

Figure 11 *Penetration ratio in dB versus grazing angles using synthetic replica*

It can be observed that, for grazing angles larger than critical, the obtained penetration ratio shows a roughly linear decrease with frequency (0.5 dB/λ) which is in agreement with the common assumption of a given dB/λ attenuation factor.

For all grazing angles below the nominal critical angle, it can be observed that the penetration ratio is highly dependent on frequency. Two main regimes can be identified:

- Below 5-7 kHz

  In this frequency range, a roughly linear decrease of the penetration ratio with frequency is observed. Also, the magnitude of slope of the curve is increasing with the decreasing grazing angle. It may be observed that significant amounts of energy are penetrating in the bandwidth 2-3 kHz, even for low grazing angles.

- Above 5-7 kHz

  In this frequency range, the obtained penetration ratio has leveled aout, and is increasing with frequency, in some cases.

3.3.2 Broadband penetration ratio into the sediment

The broadband transmission into the sediment has also been measured by integrating the received signal over the pulse duration (0.25 ms) [15].

In Annex B.1, a complete description of the variation of the SPL obtained on the different hydrophones for both the low-frequency and the high frequency of the parametric sonar may be found. The variation of the SPL is given as a function of the grazing angle for different transmitted signals.

Taking into account the results given in Annex B.1 the broadband penetration ratio has been computed and shown in Fig 12.

The following remarks can be made in regard to the broadband penetration ratio versus grazing angle:

- For both the low-frequency and the high-frequency of the signals the attenuation is changing strongly with the grazing angle.
- For the low-frequency the penetratio ratio slope is linear in grazing angle, with changing proportionally with the burial depth of the hydrophone.
- A big difference is observed between the low-frequency and the high-frequency. For example, differences of 8dB and 18dB are respectively observed for grazing angles of 32 and 22 degrees between the low-frequency and the high-frequency. Therefore, it was decided that only the low-frequency will be considered in the rest of the document for the comparison between the data and the models.

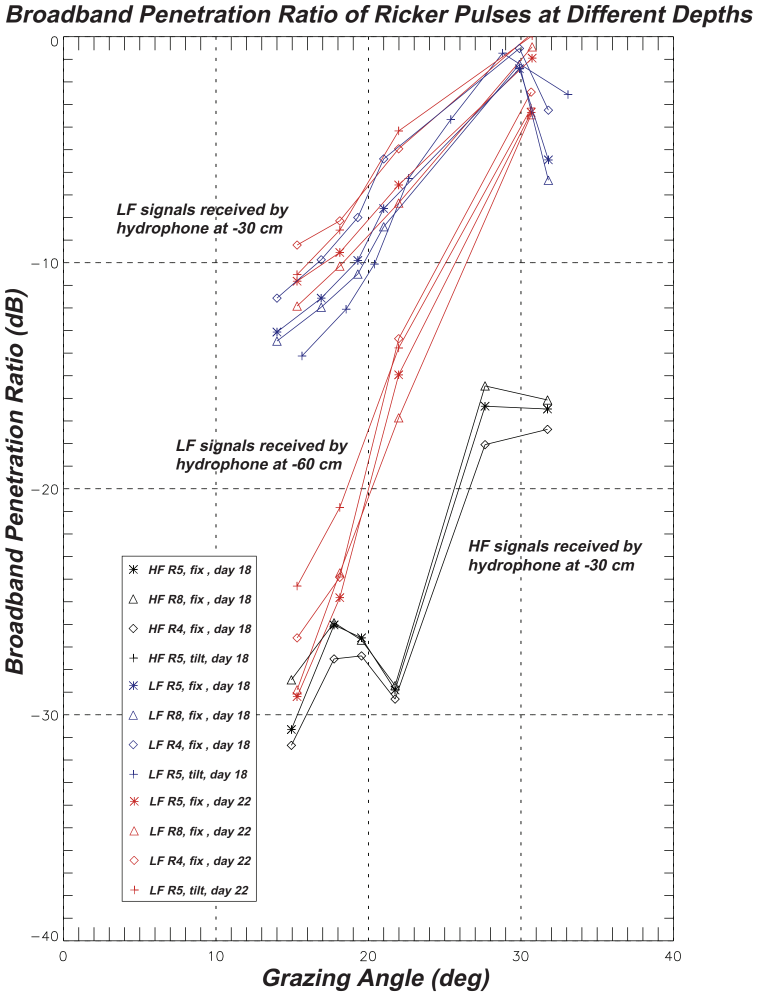

Figure 12 *Broadband penetration ratio versus grazing angle and burial depth*

4

Comparison of situ data with models

4.1 Models description

The analysis of the experimental penetration data has been performed using two new models, based on different approximations to the handling of the bottom penetration problem. Both models include the evanescent coupling as well as the roughness scattering contribution but one uses a low-frequency approximation for modeling the scattering contribution, while the other uses a a high-frequency approximation. The frequencies involved in the experiments are in the transition region between the two approximations, and the performance of either modeling approach was uncertain.

In addition, neither of the models have earlier been compared against other models or experimental data for the penetration problem, and the present study therefore also served an important model validation purpose.

One model is OASES-3D [11], which uses wavenumber integration in combination with a perturbation approach to compute the three-dimensional coherent and scattered fields in stratified ocean waveguides with rough interface patches. The other model uses the Helmholtz-Kirchhoff theory for penetration through a rough surface [12].

Both modeling approaches differ from traditional scattering theories in not using formal averaging to achieve field statistics. Instead the scattered fields are computed deterministically using realizations of the seabed roughness statistics. In the studies performed here, both models use the same synthetic rough surfaces, with spatial characteristics similar to those observed during the experiment.

4.1.1 OASES Bottom Penetration Modeling

The 3-dimensional version of the OASES propagation model has recently been combined with a perturbational approach to allow full wave-theory modeling of the 3-dimensional field associated with bottom-interaction of narrow-beam sonars such as the TOPAS parametric source [11]. The new OASES-3D model handles consistently both the coherent component of the full waveguide field, including the evanescent bottom penetration, and the scattering produced by anisotropic seabed roughness.

As a first step, the standard OASES code is applied to compute the field in a waveguide with smooth interfaces. Subsequently, the interface scattering is computed using the perturbation approach to rough elastic interface scattering developed by Kuperman and Schmidt [21],[22]. The original perturbation theory is based on a 2-D Fourier transform formulation for interfaces of infinite extent. For computational reasons this approach is only feasible for evaluation of the scattered field in plane geometry with one-dimensional roughness [22]. However, many sonar problems are characterized by a sonar 'footprint' or 'patch' of limited extent, as is the case for example for the TOPAS, and an alternative implementation of the perturbation theory has therefore been devised, which in effect represents the insonified roughness patch as a *virtual source distribution.* The field produced by this source distribution can then be very efficiently evaluated by wavenumber integration models such as OASES using azimuthal Fourier synthesis [23].

It should be pointed out that traditional perturbation approaches are most often applied to directly predict the field statistics by formal averaging. In contrast, the approach used in OASES-3D uses a spatial realization of the roughness statistics, or a directly measured roughness patch, to generate a single field realization. However, the model is sufficiently efficient to allow for computing the field statistics using ensemble averaging.

- Coherent Field Modeling

  The coherent component of the field, including the evanescent bottom field, is computed by the OASES code [24], using standard wavenumber integration for stratified waveguides [25]. This approach expresses the field produced by a point source of time dependence $exp(-i\omega t)$ in each layer in the stratification in terms of an integral representation,

  $$\chi_\ell(r) = \int_0^\infty \left[\tilde{\chi}_\ell^+(k_r)e^{ik_z z} + \tilde{\chi}_\ell^-(k_r)e^{-ik_z z}\right] k_r J_0(k_r r) dk_r \ , \tag{2}$$

  where z and r are the depth and range coordinates, and k_r is the horizontal wavenumber. The depth-dependence of the field is represented by the exponentials, with k_z being the vertical wavenumber, defined as

  $$k_z = \begin{cases} \sqrt{k_\ell^2 - k_r^2}, & k_r \le k_\ell, \\ i\sqrt{k_r^2 - k_\ell^2}, & k_r > k_\ell, \end{cases} \tag{3}$$

  where $k_\ell = \omega/c_\ell$ is the medium wavenumber for layer ℓ. In this form, the integral representation clearly separates the field into waves *propagating* vertically in the layer ($k_r \le k_\ell$), and waves which are exponentially growing or decaying, the *evanescent* waves ($k_\ell \le k_r$), separated by the critical wavenumber $k_r = k_\ell$. The amplitudes $\chi_\ell^\pm(k_r)$ are found by matching the boundary conditions of continuous particle motion and stresses (pressure) at all interfaces in the stratification.

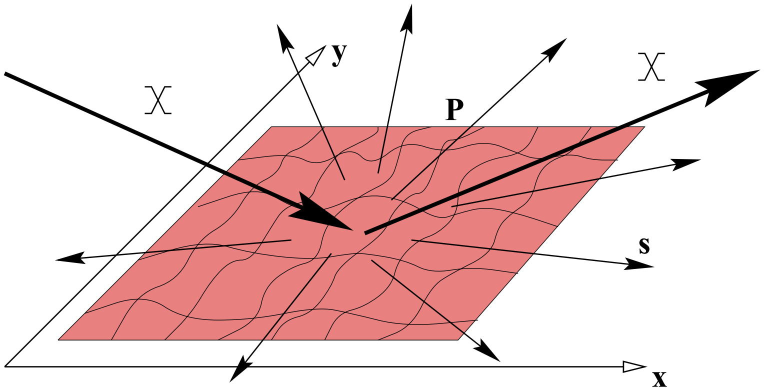

Figure 13 *Rough interface patch in stratified waveguide, insonified by a seismo-acoustic field.*

- Perturbation Scattering Theory

  Following the computation of the coherent field by wavenumber integration, the scattering by rough interfaces can be consistently handled using the method of small perturbations developed by Kuperman and Schmidt [21]. Here, the term "small" is intended with respect to the acoustic wavelength. For arbitrary fluid-elastic stratifications, this theory decomposes the wavefield into coherent and scattered components of the field potential χ_ℓ in layer number ℓ,

  $$\chi_\ell = \langle \chi_\ell \rangle + s_\ell \tag{4}$$

  Away from physical sources and the rough interfaces, the scattered potential satisfies the same homogeneous Helmholtz equations as the coherent field and the same boundary conditions. However, the physical sources are replaced by a virtual source distribution resulting from the perturbation theory as a convolution of roughness and the coherent field [21], [26],[27]

  For a finite size roughness patch or sonar footprint, the scattered field can then be represented by a spatial integral over the patch P,

  $$s(\vec{\mathbf{x}}) = \int_P G_v(\vec{\mathbf{x}}, \vec{\mathbf{x}}_v) d^2\vec{\mathbf{x}}_v \ , \tag{5}$$

  where $G_v(\vec{\mathbf{x}}, \vec{\mathbf{x}}_v)$ is a *Generalized Green's Function* satisfying the standard Helmholtz equation and the virtual source distribution.

  The result is a representation of the scattered field as an azimuthal Fourier series of wavenumber integrals given by

$$s(r,\theta) \quad = \quad \sum_{m=0}^{\infty} \left\{ \begin{array}{c} \cos m\theta \\ \sin m\theta \end{array} \right\} \int dq \, q J_m(rq)$$

$$\left[\int_P \widetilde{G}_v^m(q, r_v, \theta_v) r_v dr_v d\theta_v\right]. \tag{6}$$

4.2 Helmholtz-Kirchhoff bottom penetration modeling

This approach is based on the Kirchhoff approximation and on the Helmholtz-Kirchhoff integral. Its full description and a discussion of its validity can be found in [12]. In summary, it first analyticaly expresses the elementary pressure contribution $dp(\mathbf{R}')$ received at a fixed point $\mathbf{R}'$ within the sediment from a point $\mathbf{R}$ located on the water-sediment surface (see Fig. 14). At low grazing angle and low frequency (in this study as low as a few kHz), this approximation is only valid for gently undulating surfaces, *i.e.*, for surfaces whose ratio σ_s/l is small, σ_s being the seafloor RMS roughness and l the average correlation length. .

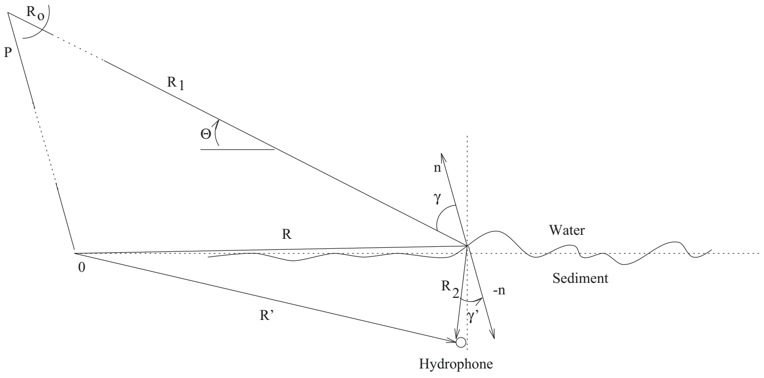

Figure 14 Geometry of measurement. The source is located at **P** and is transmitting an acoustic signal towards the seafloor. An hydrophone is located at $\mathbf{R}'$. **n** is the local normal to the surface.

Considering a directional source at P transmitting a pulse $p_0e(t)$ with a beam directivity gain $D_i(\mathbf{P}-\mathbf{R}, f)$, $dp(\mathbf{R}')$ takes the form (in the time domain):

$$\begin{aligned} dp(\mathbf{R}',\mathbf{t}) \quad = \quad & \frac{p_0R_0}{4\pi c_1R_1R_2}(1+\Re_{12}(\mathbf{R}))e'(t-\frac{R_1+\bar{n}'_2R_2}{c_1}) \\ & (\cos(\gamma(\mathbf{R}))+\bar{n}_2\cos(\gamma'(\mathbf{R}))) * \mathcal{F}^{-1}\{e^{-\frac{\alpha f R_2}{2}}\} \end{aligned}$$

$$*\mathcal{F}^{-1}\{D_i(\mathbf{P}-\mathbf{R},f)\}d\mathbf{S_R} \tag{7}$$

where $\Im_{12}(\mathbf{R}) = 1 + \Re_{12}(\mathbf{R})$ is the local water-sediment plane wave transmission coefficient, $\gamma(\mathbf{R})$ is the angle made between the incident direction and the normal vector $\mathbf{n}$ to the surface at $\mathbf{R}$, $\gamma'(\mathbf{R})$ is the angle made between the refracted direction and the normal vector **-n** to the surface at $\mathbf{R}$, $\bar{n_2'}$ is the real part of the water-sediment index of refraction, k_1 is the wave number in the water at a given frequency f, and c_1 is the average sound speed in water. The term $d\mathbf{S_R}$ corresponds to an elementary surface of the seafloor at $\mathbf{R}$. $\mathcal{F}^{-1}$ denotes an inverse Fourier transform and $*$ is the convolution factor. The term α is the attenuation term assuming a linear attenuation with frequency.

The surface ensemble (S_t) is defined as all the seafloor elementary surfaces which are seen from the source at $\mathbf{P}$ (*i.e.*, which are not in the shadow zones). The second step of the model consists a computing the total pressure field received at the hydrophone $p(\mathbf{R}',t)$ by summing all the elementary pressures $dp_{(S)}(\mathbf{P}',\mathbf{t})$ over the surface (S_t),

$$p(\mathbf{R}',t) = \int_{(S_t)} dp(\mathbf{R}',\mathbf{t}). \tag{8}$$

The computation of $p(\mathbf{R}',t)$ of Eq. (8) is based on the random generation of realistic seafloor interface height fields $z(\mathbf{R})$. Computer simulations are based on the Fourier synthesis method [20]. For each seafloor realisation, a random surface height power spectrum is generated and converted to an amplitude field in the spatial domain using a Fourier transform. Each realization has the expected first and second moments (mean values and standard deviations). The generated random power spectrum is made out of a pre-defined power roughness spectrum (gaussian or power law, for example), for which part of the phase and amplitude is randomized). Each random power spectrum produces a unique height field configuration which can be utilized for computing a single realization of the pressure field $p(\mathbf{R}',t)$ in the time domain. Figure 15 shows an example of a generated seafloor interface height field which is used in the following simulations.

4.3 Data-models comparison

4.3.1 OASES Modeling

As described above, OASES-3D computes the bottom field in two steps. The first uses wavenumber integration to compute the incident field, including the evanescent bottom field for sub-critical grazing angles. The second step then convolves this field with the roughness of the sonar footprint to yield a virtual source distribution,

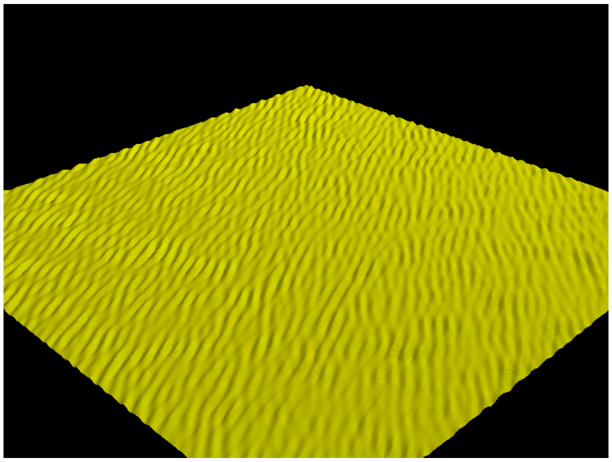

Figure 15 3-D Display of a seafloor realisation $z(\mathbf{R})$. The dimension of the generated surface is 10 m x 10 m. The RMS roughness $\sigma_s^2 = 2.5cm$. The spatial frequency K_c was put equal to $31.5rad/m$ which corresponds to a correlation length l equal to 20 cm, cut-off spatial frequency $K_{hp} = 10rad/m$.

the field produced by which is then determined using azimuthal Fourier synthesis of wavenumber integrals. Consequently, the penetration is inherently decomposed into a *coherent* component and a *scattering* component, with obvious interpretation advantages.

Figs. 16 - 19 give a comparison of the data results with the results obtained applying the OASES models. The red curve shows the predicted penetration ratio for plane wave incidence. The blue curve accounts for the finite TOPAS beamwidth. Crosses indicate the scattering contribution predicted by OASES-3D.

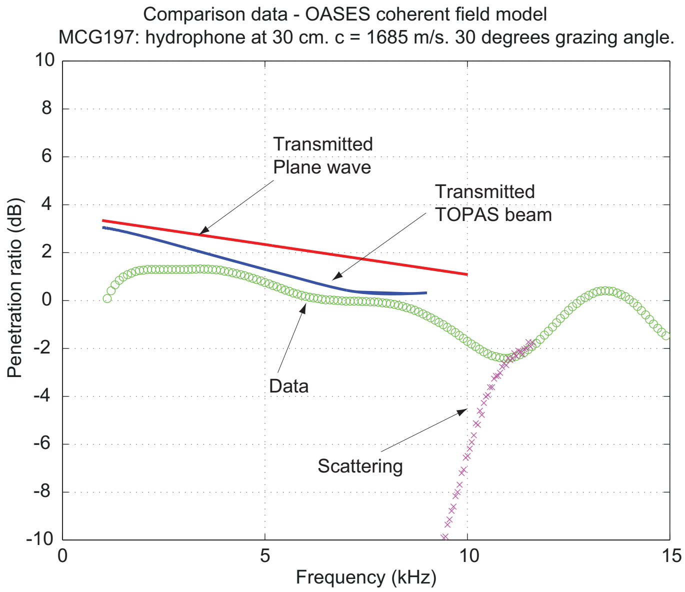

Figure 16 *Penetration ratio for hydrophone at -30cm. Grazing angle = 30 degrees. Comparison between the data and the evanescent wave model and the small perturbation model*

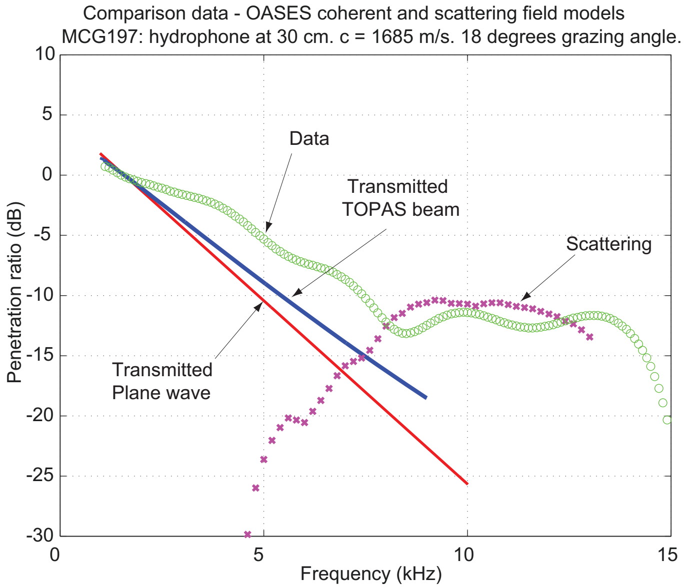

Figure 17 *Penetration ratio for hydrophone at -30cm. Grazing angle = 18 degrees. Comparison between the data and the evanescent wave model and the small perturbation model*

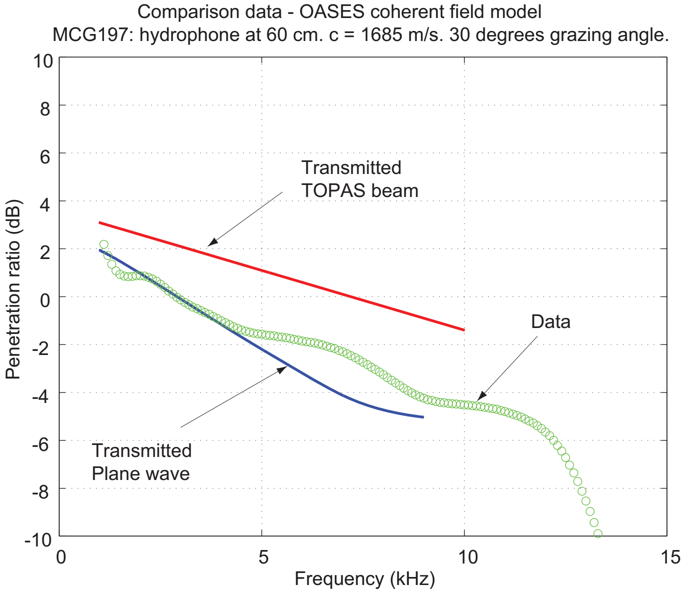

Figure 18 *Penetration ratio for hydrophone at -60cm. Grazing angle = 30 degrees. Comparison between the data and the evanescent wave model and the small perturbation model. Due to not enough high level energy, the contribution of the small perturbation model does not appear on the plot*

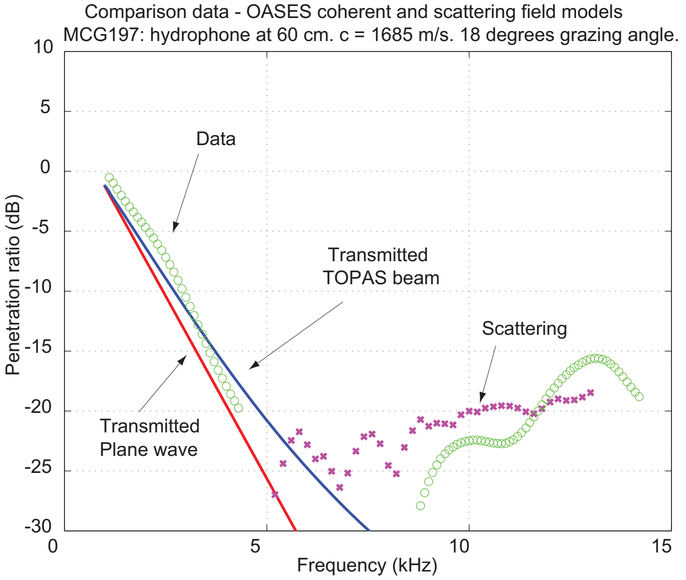

Figure 19 *Penetration ratio for hydrophone at -60cm. Grazing angle = 18 degrees. Comparison between the data and the evanescent wave model and the small perturbation model*

- Coherent Field Modeling

  The coherent field in the bottom below the TOPAS footprint is of finite spatial spectral composition, in spite of the fact that the parametric source is often considered as producing highly directional wave field, as discussed by Jensen and Schmidt [5], who analyzed the penetration problem in this context. Since OASES directly allows for modeling plane wave incidence, as well as simulating the actual spectral content of the source, both incidence field models were considered.

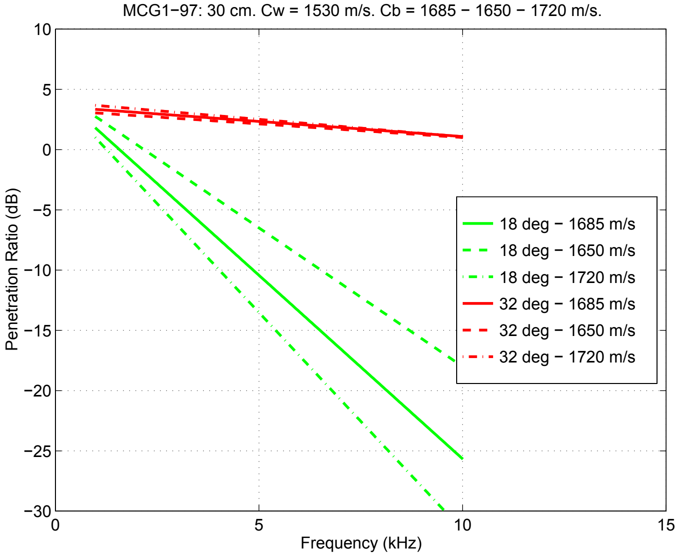

Figure 20 *Penetration ratio in dB for 30 cm deep hydrophone, for plane wave incident at* 18° *and* 32° *grazing angles. The water sound speed is 1530 m/s, while the bottom sound speed is varied. Solid: 1685 m/s; Dashed: 1650 m/s; Dashed-dotted: 1720 m/s.*

The first modeling effort used simple incident plane waves at the nominal angles of the TOPAS configuration. Fig. 20 shows as the dashed-dotted line the penetration ratio in dB for a hydrophone buried at 30 cm depth, assuming a bottom sound speed of 1720 m/s, as measured on cores at 200 kHz. The density of the sediment was measured to 1.92, and the water sound speed was 1530 m/s. The water is assumed lossless, while a compressional wave attenuation of 0.5 dB/λ was assumed for the sediment. This attenuation value resulted from the study as the one providing the best match with the data and is within reasonable values for this type of sediment.

The penetration ratio is defined as the hydrophyne pressure divided by the incident pressure in the water column in the absence of the bottom interface. This prediction fell far short of the measured data, both for this burial depth and for the deeper (60 cm) hydrophone. The bottom sound speed was therefore

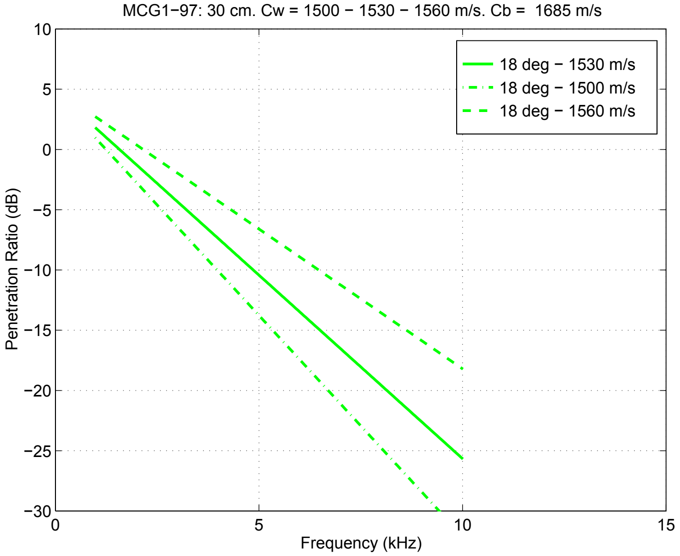

Figure 21 *Penetration ratio in dB for 30 cm deep hydrophone, for plane wave incident at* 18° *grazing angle. The bottom sound speed is fixed at 1685 m/s, while the water sound speed is varied. Solid: 1530 m/s; Dashed: 1560 m/s; Dashed-dotted: 1500 m/s.*

varied to better match the data. Fig. 20 shows several results, obtained for bottom sound speeds of 1685 m/s (solid lines) and 1650 m/s (dashed line). These results clearly shows a strong dependence on the sound speed in the bottom for subcritical incidence (18°). The reason for the high sensitivity to the bottom speed is the significant associated changes in critical angle. Thus, the fast bottom (1720 m/s) has a critical angle of $\theta_c = 27.19°$, while the slower bottoms have critical angles of $\theta_c = 24.77°$ (1685 m/s), and $\theta_c = 21.99°$ (1650 m/s). On the other hand the sound speed effect is insignificant at super-critical incidence.

The same critical angle effect is observed in Fig. 21, where the bottom speed is fixed at 1685 m/s while the water sound speed is varied. The incident angle is 18° The solid curve represents the measured sound speed of 1530 m/s ($\theta_c = 24.77°$), the dashed curve 1560 m/s ($\theta_c = 22.21°$), and the dashed-dotted curve 1500 m/s ($\theta_c = 27.10°$).

Another critical parameter is the burial depth of the hydrophone. In the experiment the nominal burial depths were 30 and 60 cm, but with the ripple structure and sediment transport during the experiment, an uncertainty of a few cm is expected. Fig. 22 shows the sensitivity of the penetration ratio for the 30 cm phone to the actual burial depth.

In addition to the sensitivity to the wave speeds and the burial depth, the sensitivity to bottom shear parameters was investigated. It was found, however,

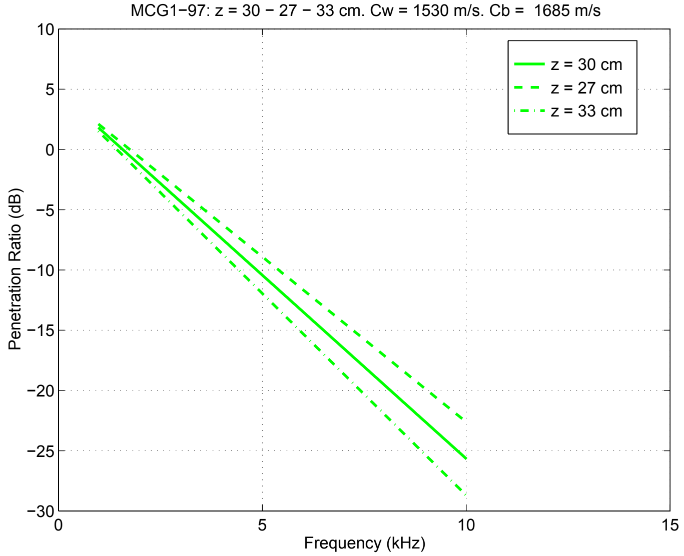

Figure 22 *Penetration ratio in dB for hydrophone at a nominal depth of 30 cm, for plane wave incident at* 18° *grazing angle. The water and bottom sound speeds are fixed at 1530 and 1685 m/s, respectively. Three actual burial depths are considered: Solid: 30 cm; Dashed: 27 cm; Dashed-dotted: 33 cm.*

that for shear speeds less than 400 m/s, as is typical for sediments, there is no significant penetration effect due to shear.

As a next step, the finite TOPAS beamwidth was considered by letting OASES model the beam using a focused vertical array [5]. It must be mentioned that the achieved beamwidth with this technique is not meant to exactly reproduce the TOPAS beamwidth and its variation with frequency. The main objective of the simulation was to be able to show qualitatively the influence of a frequency varying beamwidth on the penetration. Including this effect the best match with the data on both hydrophones was achieved for a bottom sound speed of 1685 m/s, and the water speed being the measured 1530 m/s. The result for an incident angle of 32° is shown in Fig. 16. Note that the finite beamwidth lowers the penetration ratio at this supercritical angle. The reason is that the finite beamwidth is associated with a finite spectral width. Therefore, in this case, the penetrated field is undergoing geometrical spreading, in contrast to the plane waves.

Similarly, the finite spectral width will increase the penetration ratio for subcritical angles, as indicated in Fig.17 , showing the measured data and the OASES modeling results for 18° nominal incident angle. In the sub-critical case, the higher angles of the source spectrum are closer to the critical angle, and since the evanescent coupling is exponentially decaying away from the critical angle, the resulting penetration will be higher than predicted at the nominal incident angle.

Figs. 18 and 19 show the corresponding results for the hydrophone buried at 60 cm depth. Here again the agreement between the OASES modeled coherent field and the data is excellent. Again the bottom sound speed was assumed to be 1685 m/s, and the beamwidth effect is equally evident here.

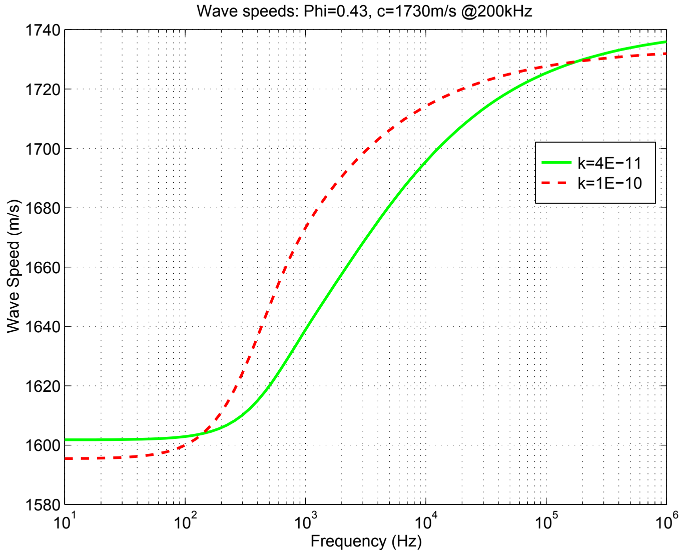

Figure 23 *Frequency dependence of sound speed in sand with porosity 43%. The two curves show the results for two different permeabilities within the range typical for this type of sand.*

In summary, the analysis of the penetration data shows that the measured seabed field at frequencies below 5-7 kHz is accurately predicted by standard spectral models, in particular when accounting for the finite spectral and spatial width of the Topas beam. However, the analysis shows a significant discrepancy between the apparent compressional speed in the bottom (1685 m/s) and the speed measured on core specimens in the laboratory (1720 m/s). To investigate whether such a frequency dependence is justifiable, the Biot-theory poro-elastic capability of OASES was used. The core analysis included porosity (44%) and grain size distribution measurements, but unfortunately the permeability, which is a very significant parameter for the frequency dependence, was not measured. OASES was therefore applied to estimate the bottom sound speed variability with frequency for a range of permeabilities historically observed for sand of this type. Fig. 23 shows the predicted sound speed variation for permeabilities of $k = 10^{-10} m^2$ and $k = 4 \times 10^{-11} m^2$. In both cases other free Biot parameters were adjusted to yield 1720 m/s at 200 kHz. These results clearly show that a compressional speed of 1685 m/s in the 1- 10 kHz regime is not unrealistic. Also, it should be pointed out that with these sediement parameters, the generated slow wave is totally insignificant to the penetration.

In fact the high sensitivity to the sediment speed suggests that the estimate provided by inversion of penetration data is much more accurate and robust than the high-frequency core estimate. This follows, of course, provided the experimental geometry is well controlled, as the sensitivity to burial depth is equally critical, as shown in Fig. 22.

It should be pointed out that OASES can predict the penetration directly using the Biot theory. However, it was desirable for interpretational purposes to operate with the much simpler equivalent fluid models.

In spite of the fact that the Biot theory may directly explain the difference of sound speed necessary to match between the data and the models, it is important to note that other explanations may be given.

Thus, as already mentioned previously, the knowledge of the accurate geometry (grazing angle, burial depth) is essential knowing that a slight change in these two parameters will have a significant influence on the measured sound pressure level.

In order to be able to completely answer the question of the variation of the sound speed with the frequency, another experiment will be conducted in May 1998 where in situ measurements of the sandy bottom permeability will be performed.

- The OASES computations of the penetration due to interface roughness is performed using the environmental parameters providing the best match for the coherent field, i.e. a water sound speed of 1530 m/s, a sediment speed of 1685 m/s, and a sediment density of 1.9 g/cm^3. The bottom attenuation was 0.5 dB/λ. The ripple field is identical to the one used for the simulations by the Helmholtz-Kirchhoff approach. It is a realization based on a model by Pouliquen and Lyons [12], approximating the ripple structure observed during the experiment, with a correlation length of 20 cm, a RMS height of 2.5 cm, and a skewness of 30° relative to the plane of incidence. The same synthetic ripple field was previouly shown in Fig. 15.

  To approximate the 3-dimensional beampattern of the TOPAS, the roughness patch is shaded by a Hanning window in both directions, as observed in Fig. 24. The scattered field is linear in the roughness height, and the patch shading is therefore equivalent to the incident beam shading within the limits of the perturbation theory.

  OASES-3D directly provides a spatial field distribution, as illustrated in Figs. 25 and 26. The figures shows the pressure field associated with the roughness scattering in horizontal planes 30 cm and 60 cm below the seabed, centered at the patch center. The pressure levels are in dB, corresponding to a 6 kHz plane wave incident at 18° grazing. Note the strongly anisotropic nature of the field, governed by the ripple skewness, and the strong variability of the scattered

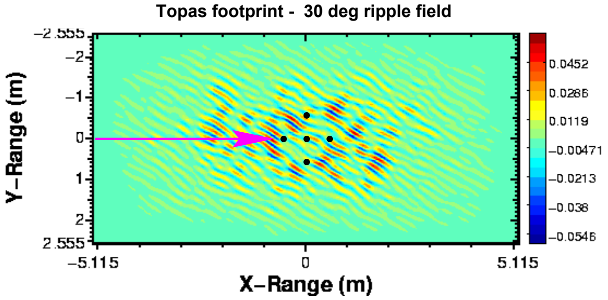

Figure 24 *Ripple field used for OASES field computations. The correlation length is 20 cm, the RMS height is 2.5 cm, and the skew angle is* 30° *relative to plane of incidence. The penetration ratio is computed as an average over a cross-array of 0.5 m spacing as indicated.*

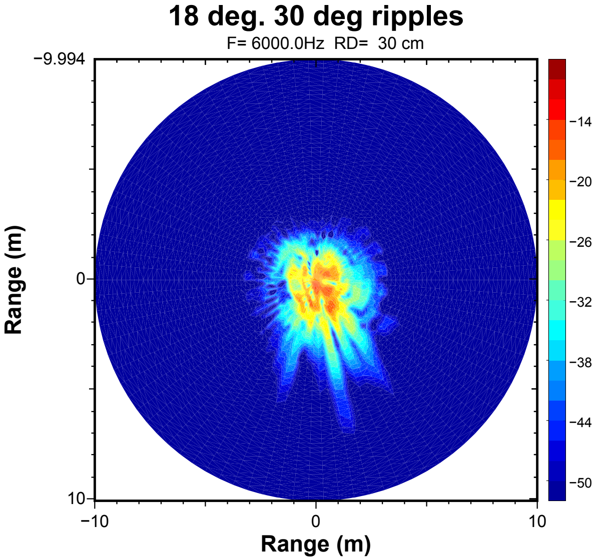

Figure 25 *Scattered acoustic pressure field in dB 30 cm into sediment below ripple seabed shown in Fig. 24. The patch is insonified by a 6 kHz plane wave of* 18° *incident angle.*

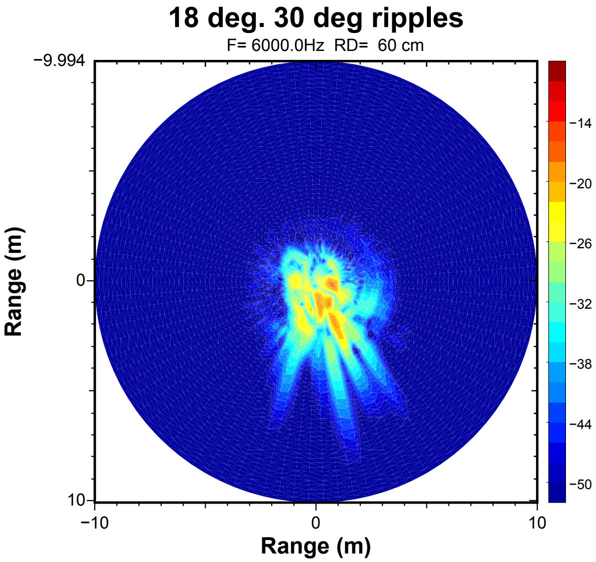

Figure 26 *Scattered acoustic pressure field in dB 60 cm into sediment below ripple seabed shown in Fig. 24. The patch is insonified by a 6 kHz plane wave of* 18° *incident angle.*

field due to interference, the acoustic equivalent to the optical 'swimmingpool effect'.

To reduce the realization-specific interference variability, the penetration ratio was determined by averaging the field over 5 hydrophone positions spaced 0.5 m in a cross configuration below the center of the patch, as indicated in Fig.24. The results are indicated by crosses (x) in Figs. 17 and 19.

The scattering predictions are obviously in excellent agreement with the measured data above 7 kHz, in particular in view of the realization-specific interference uncertainty of approximately ±3 dB.

4.3.2 Comparison of data with Helmholtz-Kirchhoff model

As described above, the 3D Helmholtz Kirchhoff model uses a stochastic approach: for a given seafloor realization, it computes the pressure signal at a single location into the seafloor. It is therefore inappropriate to directly confront data and model penetration ratios which are both the outputs of two independent random processes.

One possible way to compare data and model is to average the output of the model on several realizations and to use the averaged result as a reference. Fig. 27 presents the penetration ratio and its standard deviation for 10 different seafloor realizations, both at 30 and 18 degrees grazing angle.

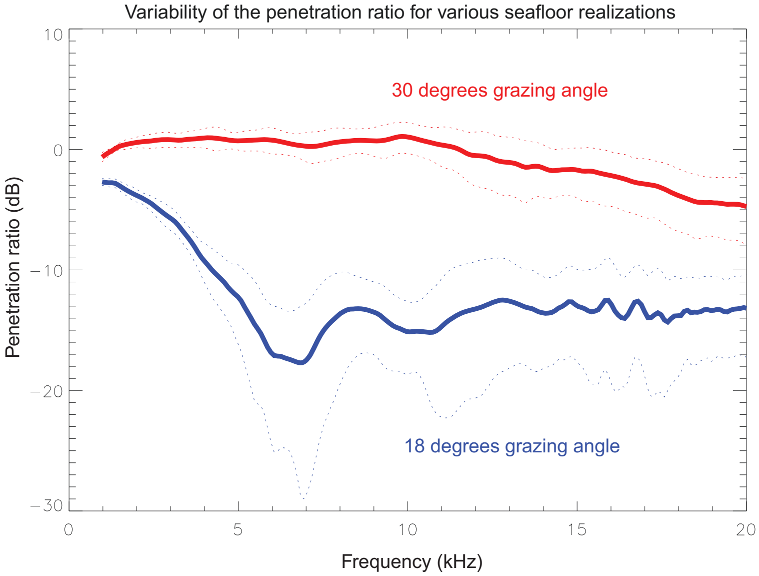

Figure 27 *Variability of the penetration ratio for various seafloor realizations using the Helmholtz-Kirchhoff model. The solid line gives the averaged penetration ratio. The dotted lines give the upper and lower bounds*

It shows that the variability of the penetration ratio is very high especially above 4 kHz where the evanescent wave becomes less dominant and the roughness scattering process gradually takes over. Expecting a close match between data and model is therefore illusive but it gives an idea on whether or not, model and data are more or less in agreement. In addition to this statistical aspect, at some frequencies (here around 7 kHz), one may find higher variability that could be caused by the seafloor surface realization used for this simulation. A given orientation of the ripple field (in our case when the ripple direction is skewed by 30 degrees) may produce destructive interferences at very particular frequencies which perturbs the penetration ratio even more.

Contrary to OASES, the Helmholtz-Kirchhoff model estimates the penetration ratio over the whole considered spectrum (2-15 kHz), combining in the same calculation the evanescent coupling effect -by respecting the Huyghens principle- with the scattering effect due to local seafloor roughness -where the Kirchhoff approximation plays its effective role-. This model produces at the hydrophone the received amplitude signal for a particular environmental and geometrical configuration.

Figs. 28 to 31 present on the same plot a data averaged penetration ratio and a simulated penetration ratio for two hydrophones located at -30 cm and -60 cm at two different grazing angles (30 and 18 degrees). The simulations have been performed using the same seafloor realization as the one used by OASES. Water and seafloor sound speed were respectively set to 1520 m/s and 1685 m/s. At sea acquisition have been performed such that the recorded signals at the hydrophones into the sediments correspond to a maximum penetration ratio. The corresponding model penetration ratios have been computed by randomly and horizontaly moving the hydrophone location for the same seafloor realization until maximum energy was found. Adequation between model and data is excellent considering their high degree of variability. However, below 5 kHz, the model penetration ratio is slightly underestimated. This can be explained in several ways:

- As shown with OASES sensitivity analysis, a slight misestimation of water sound speed, of sediment sound speed, of the burial depth of the hydrophone or of the permeability of the considered sand can lead to errors in the evanescent wave amplitude. This is inherent to environmental characterisation.
- Local seafloor topography could be causing a misevaluation of the local grazing angle. Around and below critical angle, the grazing angle plays a key role in the evanescent coupling phenomenon.
- Every parametric source has a particular directivity pattern whose temporal frequency content is particularly difficult to quantify. It is known that the beam pattern is widening as frequency goes down. In this study, the Helmholtz-Kirchhoff model uses a constant beam pattern over the 2-15 kHz range which tends to underestimate the low frequency part of the penetration ratio. This aspect will be accounted for in the future but in this report, a slight underestimation of the low frequency part of the penetration ratio by a few dB is normally expected.

In summary, the measured seabed field is well predicted using the Helmholtz-Kirchhoff approach.

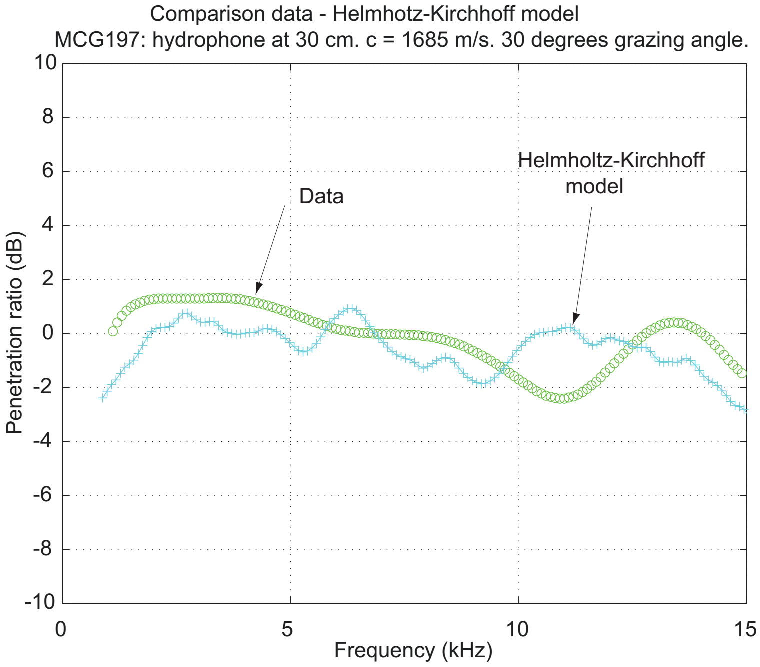

Figure 28 *Penetration ratio for hydrophone at -30cm. Grazing angle = 30 degrees. Comparison between the data and the Helmholtz-Kirchhoff model*

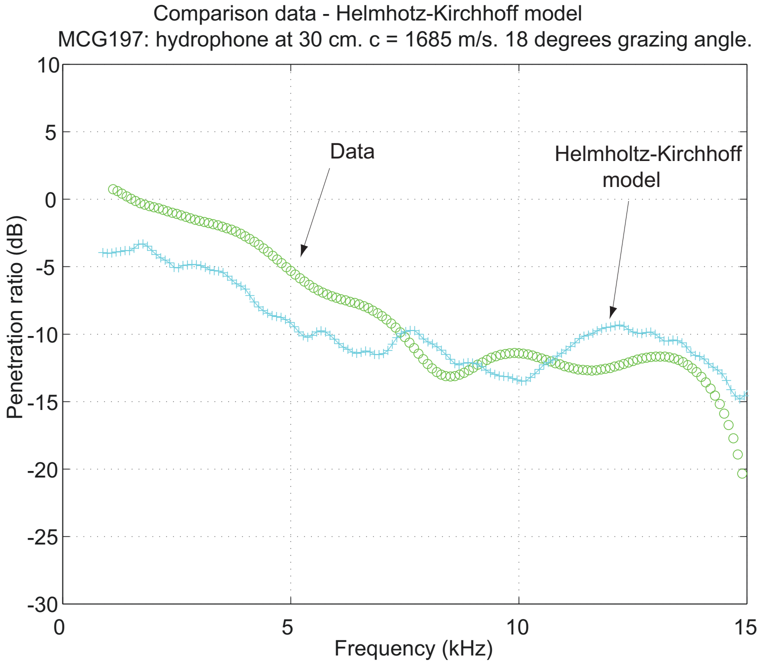

Figure 29 *Penetration ratio for hydrophone at -30cm. Grazing angle = 18 degrees. Comparison between the data and the Helmholtz-Kirchhoff model*

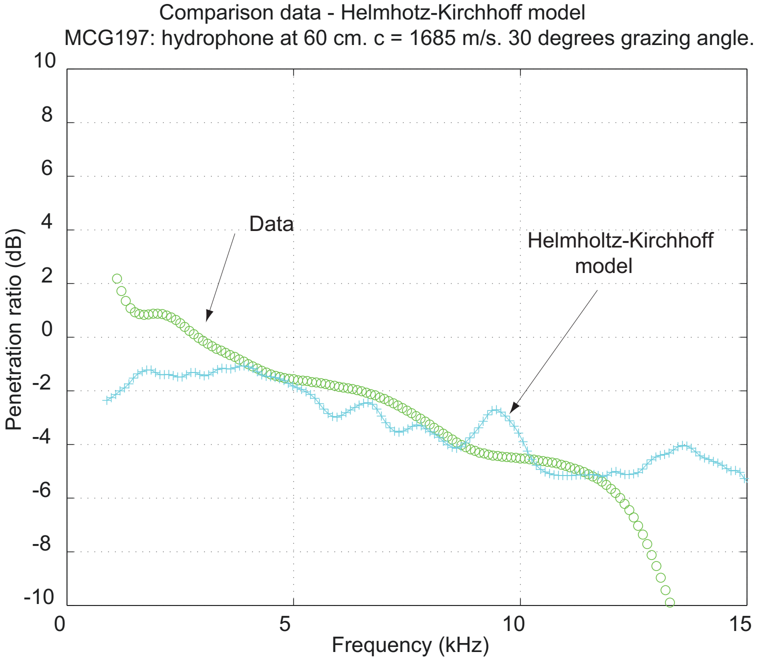

Figure 30 *Penetration ratio for hydrophone at -60cm. Grazing angle = 30 degrees. Comparison between the data and the Helmholtz-Kirchhoff model*

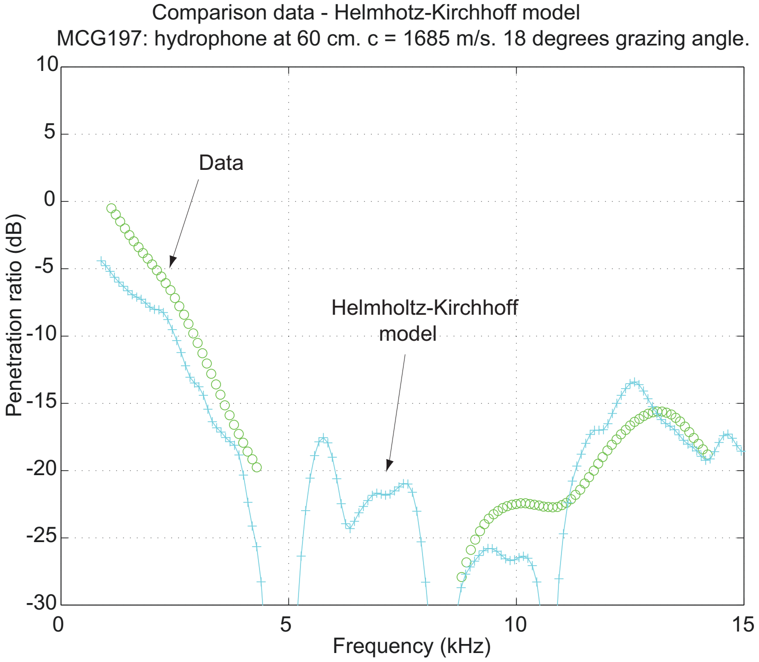

Figure 31 *Penetration ratio for hydrophone at -60cm. Grazing angle = 18 degrees. Comparison between the data and the Helmholtz-Kirchhoff model*

4.3.3 Overall comparison of data with models

Figs. 32 and 33 give an overall comparison at the two burial depths between the data and the models. Two different grazing angles, one above the critical angle and one below the critical angle, are considered.

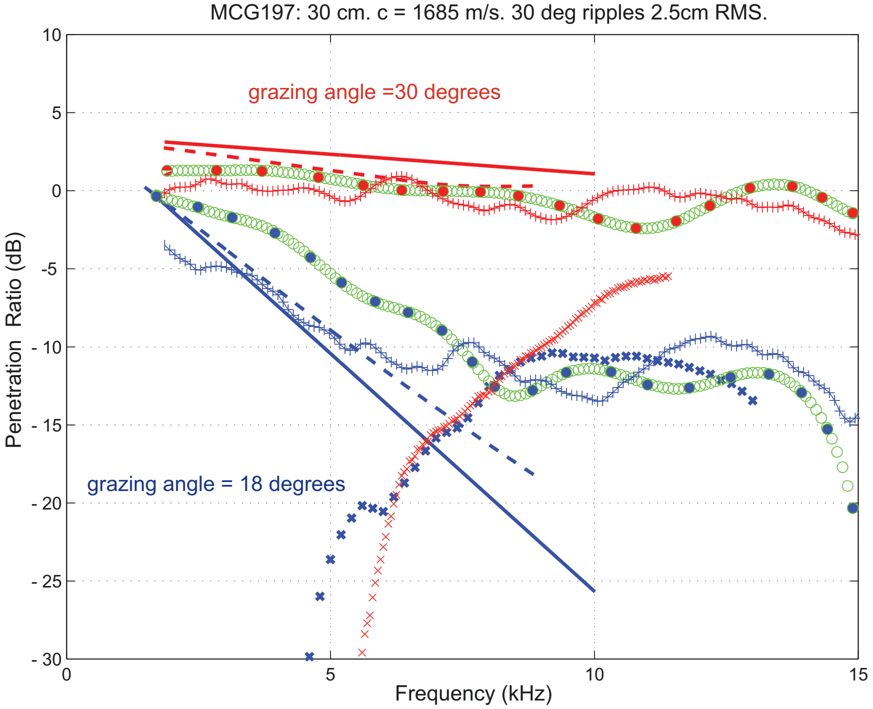

Figure 32 *Measured and modeled Penetration Ratio for hydrophone at -30cm*

The high level of consistency between the two models and the excellent agreement with the data strongly supports the conclusion that two different mechanisms are responsible for the bottom penetration for sub-critical incident angles.

For low-frequencies (up to 5-7 kHz), the main contribution to the penetrated field is associated with direct evanescent coupling with the incident field. For higher frequencies the roughness scattering appears to be the dominant mechanism. Note that OASES inherently decomposes the two components, while the Helmhotz-Kirchhoff approach provides the total field.

Another experiment with 13 hydrophones buried into the sediment (up to 50cm) was performed in November-December 1997 in a much more controlled geometry. Preliminary results show the same important conclusion concerning the predominance of the evanescent wave contribution under 5-7 kHz and the roughness scattering above this frequency.

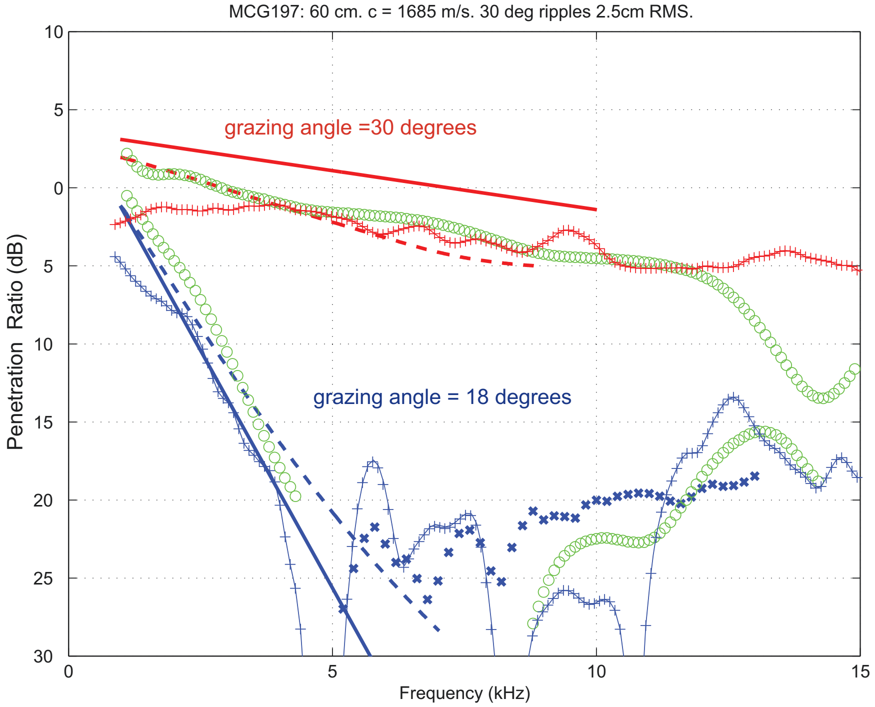

Figure 33 *Measured and modeled Penetration Ratio for hydrophone at -60cm*

5

Conclusion and future work

This report has described an initial attempt to determine the cause of sound penetration into sediments in the frequency band [2-15 kHz] and to quantify the amount of energy received on buried hydrophones while working below the critical angle. The comparison between the data and the models dealing with the evanescent wave and the roughness scattering strongly suggest, for this bottom type, the presence of two main mechanisms, the relative significance of which depends on the frequency range.

For low-frequency (up to 5-7 kHz for the considered seabed), the main contribution to the penetration is the evanescent coupling in combination with the finite beamwidth effect, while for higher frequencies the roughness scattering appears to be the dominant mechanism. Also, it was found that the frequency dependence of the sound speed in porous sand may have to be accounted for. However, it must be mentioned that the contribution of the roughness scattering was always found to be lower than the one obtained at lower frequency with direct evanescent coupling.

Therefore, in terms of the hypotheses stated in the introduction this study concludes:

- 1. Two different scattering modeling approaches adequately predicts the observed penetration above 7 kHz, suggesting that the seabed scattering hypothesis is valid at higher frequencies.
- 2. The finite beamwidth effect is significant at frequencies below 5-7 kHz, i.e, in the regime where the direct evanescent coupling is dominant.
- 3. The presence, of a second "slow" compressional Biot slow wave was not investigated during the experiment. However, no evidence of the presence of the slow wave was found in the data. On the other hand, it was found that the Biot theory predicts a frequency dependence of the fast wave speed which is consistent with the observations.
- 4. The models account for all the scattering observed, suggesting that volume inhomogeneities are insignificant in regards to the penetration in this environment and frequency regime.

As already mentioned, another experiment was performed in November-December 1997 with more hydrophones (13 instead of 2) buried into the sediment (up to 50cm) in a much more controlled geometry. Preliminary results show the same important conclusion concerning the predominance of the evanescent wave contribution at low-frequency and the roughness scattering at higher frequencies.

It was also observed that significant amounts of energy are penetrating in the bandwidth 2-3 kHz, even for low grazing angles, which may suggest a benefit from of using sonars in this frequency range for the detection of buried objects.

It must be mentioned that, to our knowledge, it is the first time that a quantification of the contributions of the roughness scattering and of the evanescent wave to the penetration into the sediment were obtained from an at-sea experiment. Moreover, the obtained results were validated using two different models with a high degree of consistency. As such, the study has also provided an important model validation result.

Future work will be dedicated to the validation of this result by proceeding to an extensive data processing of the data collected during the cruise of November-December 1997. The geometry (roughness spectrum, hydrophones burial depths, ...) being known much more accurately, the comparison of the data to the models will provide a more solid validation of the conclusions of this study. Particular attention will be given to the measurement of the spatial coherence between all the hydrophones buried into the sediment, for both the supercritical and subcritical cases. For the supercritical case, the coherence of the signals will be measured taking into account the full bandwidth, knowing that a possible loss of spatial coherence given by the bottom roughness will directly impact the array gain achieved by broadband beamforming techniques or synthetic aperture processing for the detection of buried mines. For the subcritical case, the coherence of the signals will be measured in the frequency regime for which the contribution of the roughness scattering predominates over the coherent evanescent wave, in order to evaluate the potential of using this "anomalous" energy for the detection of buried mines.

6

Acknowledgments

I would like to thank the Manning crew for their help and their constant availability during the experiement. They contribute a lot to the success of the cruise and therefore to the quality of the data collected.

The Engineering Technology Division did a great job, not only during the cruise but also before the cruise. I would like particularly to thank: P.A.Sletner who, as Engineering coordinator, succeeded to put the different systems together and to have them working perfectly during all the cruise, A.Figoli for setting up the hydrophones and the data acquisition electronics, R.Chiarabini for assuring the good functioning of the TOPAS system. The contribution of E.Michelozzi and L.Gualdesi for some days, the first one for the boomer survey and the second one for the preparation and the deployment of the rail on the bottom were also very important.

The divers team composed of scientific divers from the Centre (M.Paoli and J.Staveley) and external divers from an external company in Elba was essential for the finding of the best location of the rail, and thereafter the deployment of all the rail equipment, hydrophones and cables.

Eventually, many thanks to the reviewers (N.Pace, M.Pinto and A.Lyons) of this report who, thanks to their pertinent remarks, definitely increase its quality and readibility.

References

references in TOC (DAA, 2/97)

[1] L. M. Brekhovskikh, *Waves in Layered Media.* New York: Academic Press, second ed., 1980.

[2] J. L. Lopes, "Observations of anomalous acoustic penetration into sediment at shallow grazing angles," *Journal of the Acoustical Society of America*, vol. 99, pp. 2473–4, Apr. 1996. (Abstract).

[3] N. P. Chotiros, A. M. Mautner, A. Løvik, Å. Kristensen, and O. Bergem, "Acoustic penetration of a silty sand sediment in the 1–10-khz band," *IEEE Journal of Oceanic Engineering*, vol. 22, pp. 604–15, Oct. 1997.

[4] E. I. Thorsos, D. R. Jackson, J. E. Moe, and K. L. Williams, "Modeling of subcritical penetration into sediments due to interface roughness," in *High Frequency Acoustics in Shallow Water* (N. G. Pace, E. Pouliquen, O. Bergem, and A. P. Lyons, eds.), no. CP-45 in SACLANTCEN Conference Proceedings Series, pp. 563–9, NATO SACLANT Undersea Research Centre, June 1997.

[5] F. B. Jensen and H. Schmidt, "Subcritical penetration of narrow Gaussian beams into sediment," *Journal of the Acoustical Society of America*, vol. 82, pp. 574–9, Aug. 1987.

[6] N. P. Chotiros, "Biot model of sound penetration in water saturated sand," *Journal of the Acoustical Society of America*, vol. 97, pp. 199–214, Jan. 1995.

[7] D. R. Jackson, K. B. Briggs, K. L. Williams, and M. D. Richardson, "Tests of models for high-frequency seafloor backscatter," *IEEE Journal of Oceanic Engineering*, vol. 21, pp. 458–70, Oct. 1996.

[8] A. N. Ivakin and Y. P. Lysanov, "Theory of underwater sound scattering by random inhomogeneities of the bottom," *Soviet Physics Acoustics*, vol. 27, pp. 61–4, Jan.-Feb. 1981.

[9] P. C. Hines, "Theoretical model of acoustic backscattering from a smooth seabed," *Journal of the Acoustical Society of America*, vol. 88, pp. 325–34, July 1990.

[10] A. L. Lyons, A. L. Anderson and F. S. Dwan , "Acoustic scattering from the sea floor: Modeling and data comparison," *Journal of the Acoustical Society of America*, vol 95, pp. 2441-2451, May. 1994.

[11] H. Schmidt, J. Lee, H. Fan, and K. LePage, "Multistatic bottom reverberation in shallow water," in *High Frequency Acoustics in Shallow Water* (N. G. Pace, E. Pouliquen, O. Bergem, and A. P. Lyons, eds.), no. CP-45 in SACLANTCEN Conference Proceedings Series, pp. 475–81, NATO SACLANT Undersea Research Centre, June 1997.

[12] E. Pouliquen, A. P. Lyons, N. G. Pace. "Penetration of acoustic waves into sandy seafloor at low grazing angles: The helmhotz-Kirchoff approach," tech. rep. SM290, NATO SACLANT Undersea Research Centre report, La Spezia, Italy, 1998. (in prep.).

[13] Bentech Subsea AS, Stjørdal, Norway, *TOPAS PS040 Operator Manual.*

[14] S. Fioravanti, A. Maguer, W. L. J. Fox, L. Gualdesi, and A. Tesei, "Underwater rail facility for highly controlled experiments at sea." Submitted to Third European MAST Conference, Lisbon, Portugal, 1998.

[15] O. Bergem and N. G. Pace, "Calibration of the TOPAS PS040. Part I: Measurements recorded with TOPAS acquisition system," M-119, NATO SACLANT Undersea Research Centre, La Spezia, Italy, Jan. 1996.

[16] D. J. Wingham, N. G. Pace, and R. V. Ceen, "An experimental study of the penetration of a water-sediment interface by a parametric beam," *Journal of the Acoustical Society of America*, vol. 79, pp. 363–74, Feb. 1986.

[17] J. S. Bendat and A. G. Piersol, *Engineering Applications of Correlation and Spectral Analysis.* New York: John Wiley and Sons, 1980.

[18] R. J. Urick, *Principles of Underwater Sound.* New York: McGraw Hill, third ed., 1983.

[19] C. S. Clay and H. Medwin, *Acoustical Oceanography: Principles and Applications*, ch. 10, appendix 10. New York: Wiley, 1970.

[20] M. F. Barnsley, R. L. Devaney, B. B. Mandelbrot, H. O. Peitgen, D. Saupe, and R. F. Voss, *The Science of Fractal Images.* New York: Springer-Verlag, 1988.

[21] W. A. Kuperman and H. Schmidt, "Self-consistent perturbation approach to rough surface scattering in stratified elastic media," *Journal of the Acoustical Society of America*, vol. 86, pp. 1511–22, Oct. 1989.

[22] H. Schmidt and W. A. Kuperman, "Spectral representations of rough interface reverberation in stratified ocean waveguides," *Journal of the Acoustical Society of America*, vol. 97, pp. 2199–209, Apr. 1995.

[23] H. Schmidt and J. Glattere, "A fast field model for three-dimensional wave propagation in stratified environment based on the global matrix method," *Journal of the Acoustical Society of America*, vol. 78, pp. 2105–14, Dec. 1985.

[24] H. Schmidt, *OASES: Version 2.1. User Guide and Reference Manual.* Massachusetts Institute of Technology, 1997.

[25] F. B. Jensen, W. A. Kuperman, M. B. Porter, and H. Schmidt, *Computational Ocean Acoustics.* New York: AIP Press, 1994.

[26] K. LePage, *Elastic Scattering in Oceanic Waveguides.* PhD thesis, Massachusetts Institute of Technology, Jun. 1992.

[27] B. H. Tracey and H. Schmidt, "Seismo-acoustic field statistics in shallow water," *IEEE Journal of Oceanic Engineering*, vol. 22, pp. 317–31, Apr. 1997.

[28] H. Fan, *Wave theory modelling of three-dimensional seismo-acoustic reverberation in ocean waveguides.* PhD thesis, Massachusetts Institute of Technology, Sep. 1995.

Annex A

TOPAS low-frequency and high-frequency beampatterns

A.1 TOPAS low-frequency beam pattern

During the moving tilt experiment the secondary frequency signals received on the hydrophones were filtered in the signal band, then squared and integrated over the pulse duration (as in [15]) to measure the sound pressure level (SPL) as a function of the tilt angle of the pan and tilt unit.

Fig. 34 shows the SPL versus tilt angle for all positions of the rail on June 22nd .

Each plot on this figure corresponds to a different position on the rail and therefore to a different grazing angle. For each plot, three curves the variation of the signals respectively recieved on the hydrophone in the water column (60cm above the sea bottom in the water column), the hydrophone buried at -30cm and the hydrophone buried at -60cm.

On theses curves it can be observed that the grazing angle for which the maximum is achieved on each of the 3 hydrophones is sligtly changing from one hydrophone to another. This is of course due to the geometry.

Moreover, it can also be observed that the Sound Pressure Level obtained on the hydrophones for different grazing angles is drastically decreasing for the hydrophone buried at -60cm as long as the grazing angle is decreasing.

A.2 TOPAS high-frequency beam pattern

Fig. 35 shows the primary frequency beampattern measured on the hydrophones for all rail positions.

It should be noted that the high-frequency TOPAS beampattern is not symmetric, which is quite strange taking into account that the transducer is symetrical.

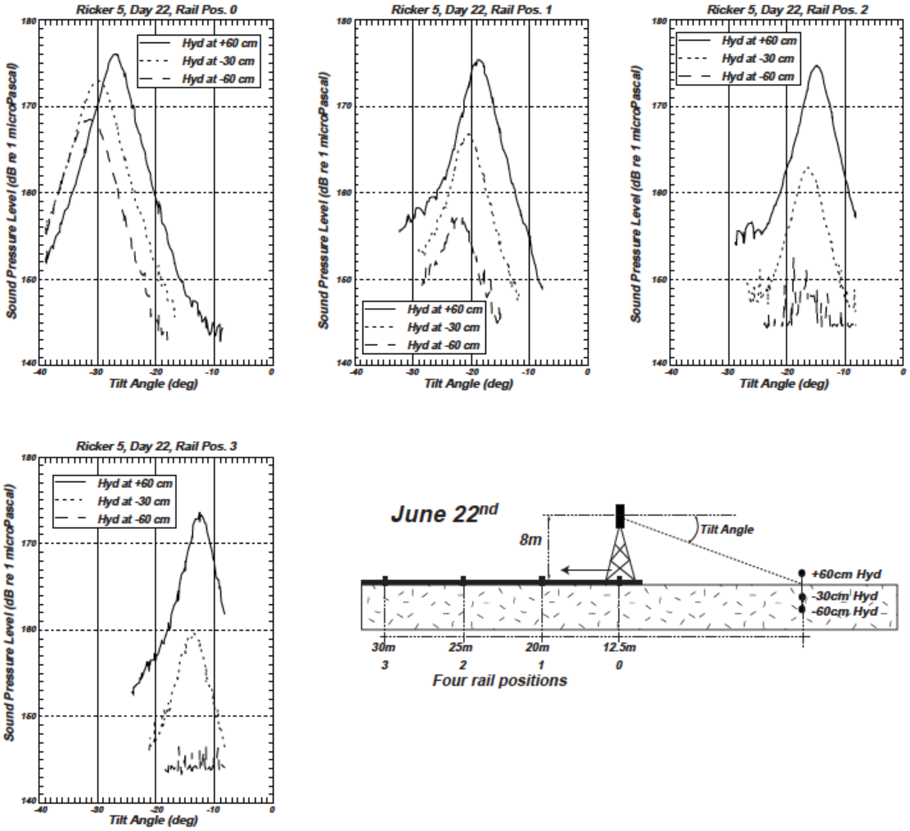

Figure 34 *Secondary Frequency SPL versus tilt angle for all rail positions on June 22nd*

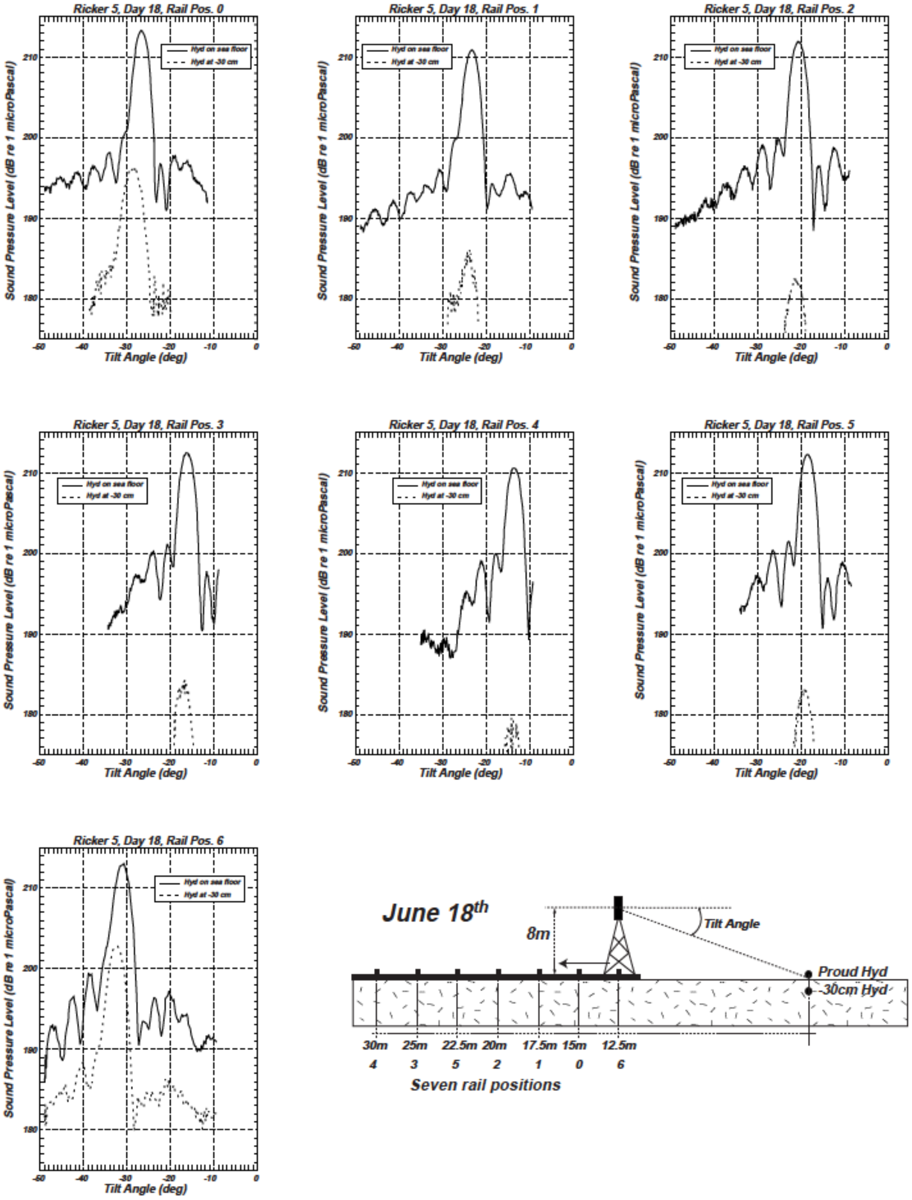

Figure 35 *Primary Frequency SPL versus tilt angle for all rail positions on June 18th*

Annex B

Variation of Sound pressure Levels in function of range and grazing angles

In reporting SPL for signals received on the buried hydrophones, we have used the calibrated sensitivities of the hydrophones as they were measured in water. It is expected that the actual sensitivities while buried in sand are not too different from those in water, but this is an issue of continuing work. However, since the sensitivities were measured in water, conversion from volts-squared to dB re 1 uPa must account for the ρ-c change of the medium ([18], where rho is the density and c is the sound speed.

B.1 low-frequency results:

Fig. 36 gives the varaition SPL obtained on the different hydrophones for both the low-frequency of the parametric sonar. The variation of the SPL is given as a function of the grazing angle for different transmitted signals.

In order to be able to compute the attenuation into the sediment (including the loss at the interface water-sand), calibrated values of the SPL expected if the received hydrophones were in the water column instead of the sediment were needed.

Fig. 37 gives the variation of the SPL as a function of the range, and effectively, of the grazing angle. On Fig. 37, giving the SPL of the low-frequency of the TOPAS it can be found the comparison of the obtained SPL with the Spherical spreading hypothesis. It can be observed, that the spherical spreading hypothesis is valid around the 35meters range whatever the frequency of the Ricker pulses used (in agreement with [15]).

B.2 High-frequency results:

Fig. 38 gives the SPL obtained on the different hydrophones for both the high frequency of the parametric sonar. The variation of the SPL is given as a function of the grazing angle for different transmitted signals.

In order to be able to compute the attenuation into the sediment (including the loss at the interface water-sand), calibrated values of the SPL expected if the received hydrophones were in the water column instead of the sediment were needed.

Fig. 39 gives the variation of the SPL as a function of the range, and effectively, of the grazing angle.

On Fig. 39, the spherical spreading assumption is of course valid at closer range for the primary frequency of the parametric sonar.

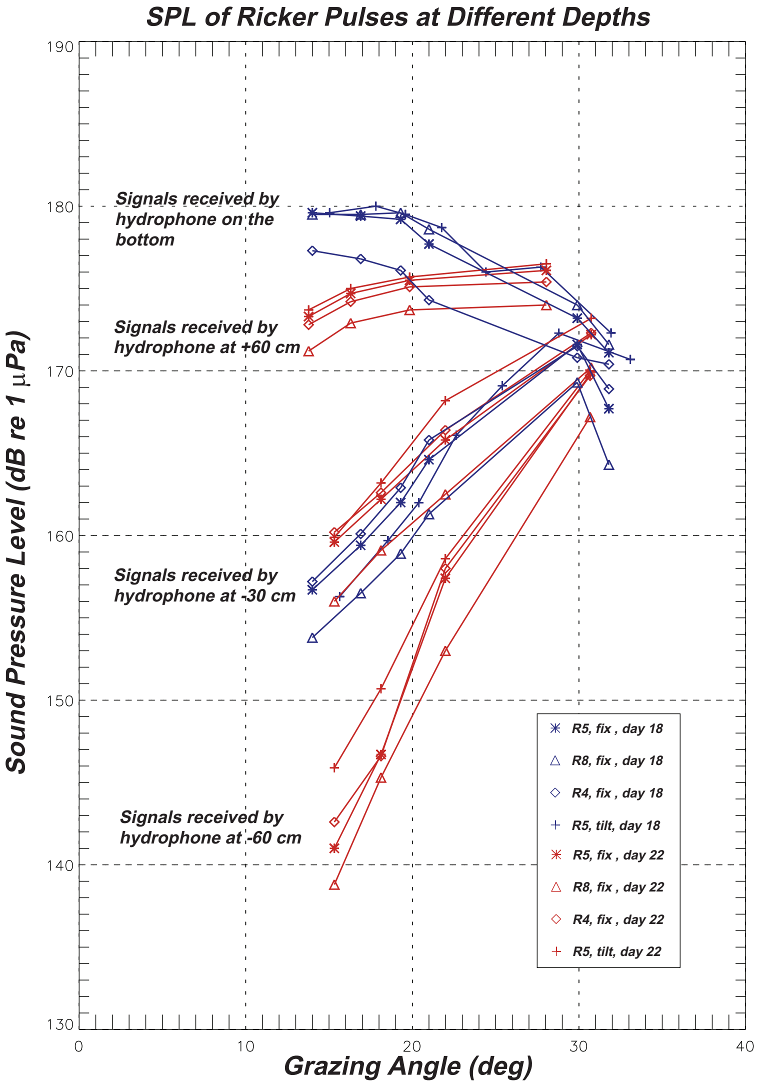

Figure 36 *Low-frequency SPL vs depth and grazing angle*

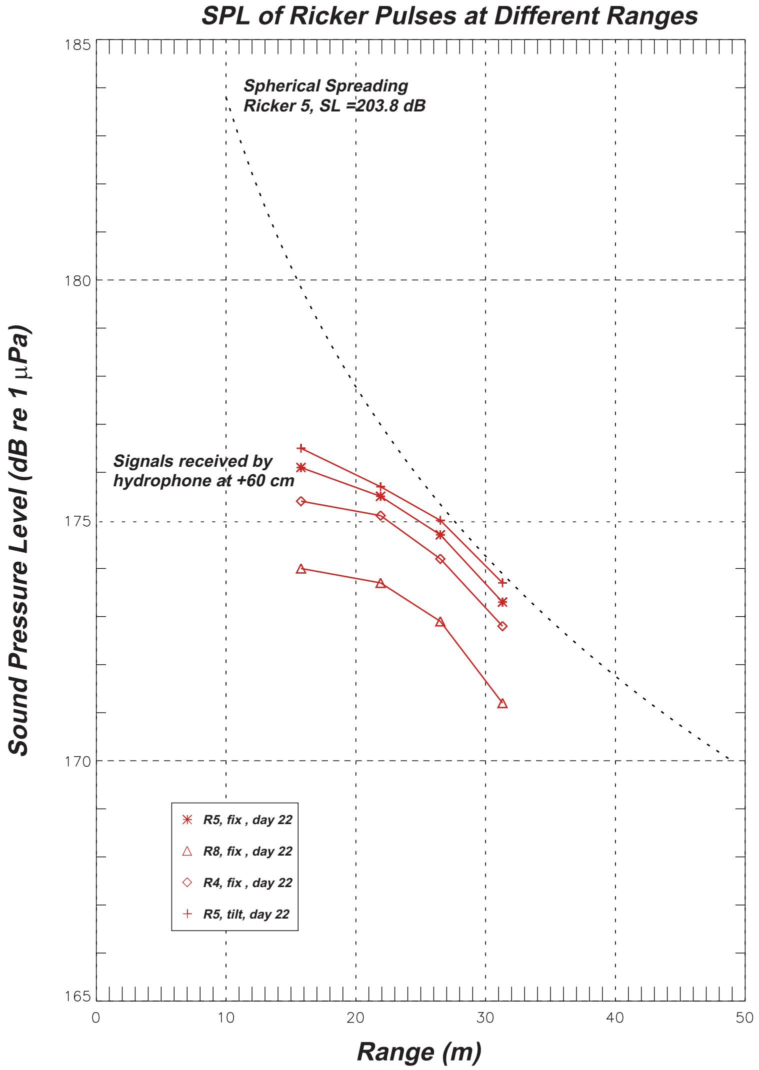

Figure 37 *Low-frequency SPL vs range*

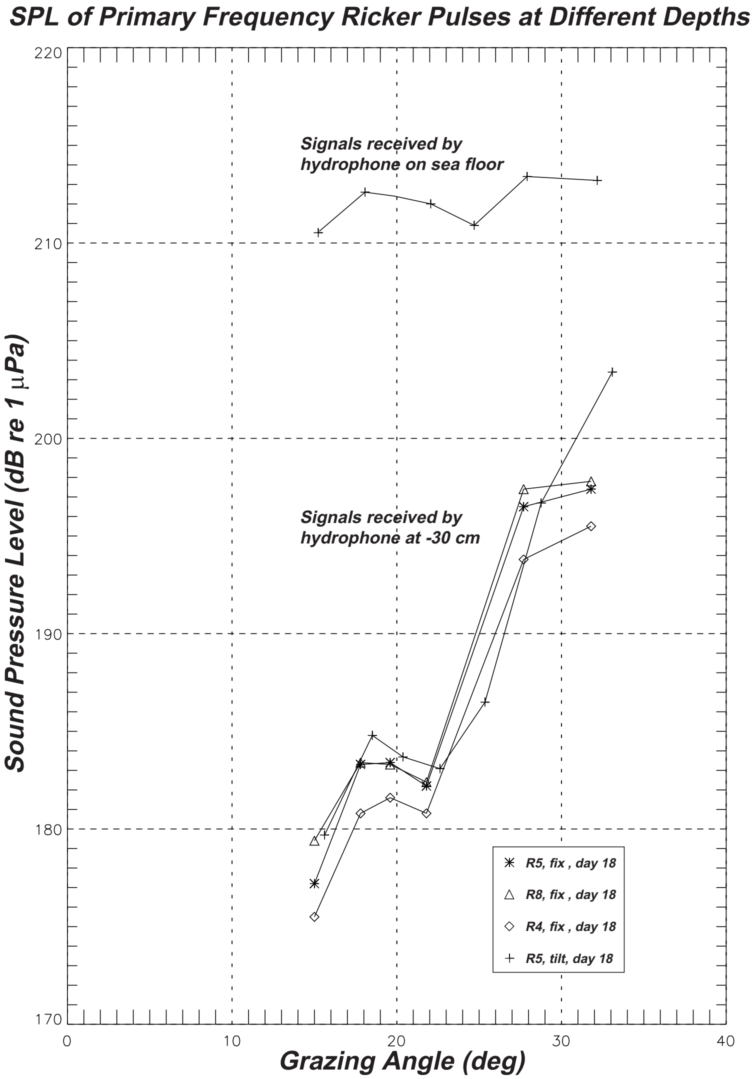

Figure 38 *High-frequency SPL vs depth and grazing angle*

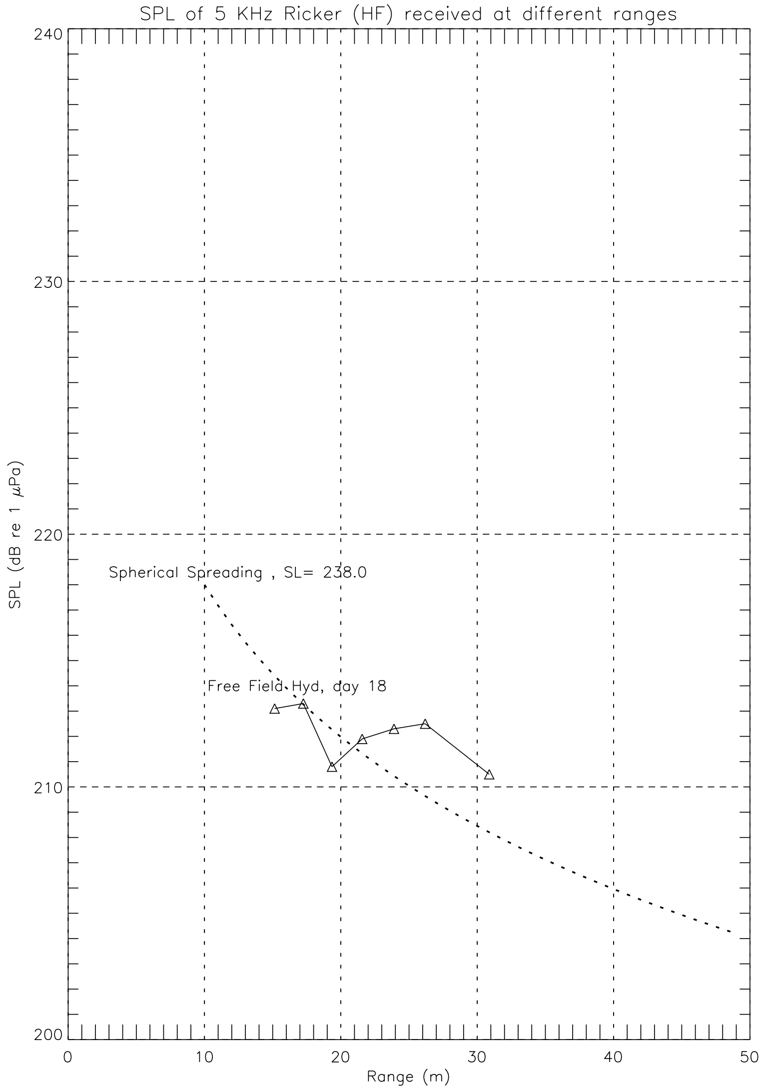

Figure 39 *High-frequency SPL vs range*

Report no. changed (Mar 2006): SR-287-UU

NATO Undersea Research Centre
Viale San Bartolomeo 400
19138 La Spezia, Italy